

Coinfection by influenza A virus and respiratory syncytial virus produces hybrid virus particles

Received: 10 August 2021

Accepted: 2 September 2022

Published online: 24 October 2022

 Check for updates

Joanne Haney¹, Swetha Vijaykrishnan¹, James Streetley², Kieran Dee¹, Daniel Max Goldfarb¹, Mairi Clarke², Margaret Mullin³, Stephen D. Carter¹, David Bhella^{1,2} and Pablo R. Murcia¹✉

Interactions between respiratory viruses during infection affect transmission dynamics and clinical outcomes. To identify and characterize virus–virus interactions at the cellular level, we coinfecting human lung cells with influenza A virus (IAV) and respiratory syncytial virus (RSV). Super-resolution microscopy, live-cell imaging, scanning electron microscopy and cryo-electron tomography revealed extracellular and membrane-associated filamentous structures consistent with hybrid viral particles (HVPs). We found that HVPs harbour surface glycoproteins and ribonucleoproteins of IAV and RSV. HVPs use the RSV fusion glycoprotein to evade anti-IAV neutralizing antibodies and infect and spread among cells lacking IAV receptors. Finally, we show that IAV and RSV coinfection in primary cells of the bronchial epithelium results in viral proteins from both viruses co-localizing at the apical cell surface. Our observations define a previously unknown interaction between respiratory viruses that might affect virus pathogenesis by expanding virus tropism and enabling immune evasion.

Viruses are intracellular pathogens whose replication relies on the infection of a restricted subset of cell types, a property known as tropism. As multiple viruses exhibit the same tropism, cells and tissues are susceptible to infection by a community of taxonomically diverse viruses. From this perspective, a tissue or body compartment constitutes an ecological niche in which members of a virus community co-exist. Coinfections by more than one virus represent between ~10–30% of all respiratory viral infections and are common among children^{1,2}. The clinical impact of viral coinfections is unclear: while some studies indicate that coinfections do not alter the outcome of disease^{3–5}, others report increased incidence of viral pneumonia^{6,7}.

At the cellular level, the interactions that determine the outcome of coinfections are unclear. Direct interactions between viruses within

coinfecting cells can result in changes to viral progeny, including, but not limited to, pseudotyping (incorporation of surface proteins from a different virus)^{8–10} or genomic rearrangements, which may generate novel strains with pandemic potential such as SARS-CoV-2 and pandemic influenza A viruses^{11,12}.

Here we examined interactions between two commonly co-circulating viruses of clinical importance: IAV and RSV. IAV causes over five million hospitalizations each year¹³ and RSV is the leading cause of acute lower respiratory tract infection in children under five years of age^{14,15}. To study virus–virus interactions during coinfection, we infected a cell line derived from human lung (A549)¹⁶, with a mixed inoculum of IAV and RSV, or individual viruses as controls.

¹MRC-University of Glasgow Centre for Virus Research, School of Infection and Immunity, College of Medical, Veterinary and Life Sciences, University of Glasgow, Glasgow, Scotland, UK. ²Scottish Centre for Macromolecular Imaging, College of Medical, Veterinary and Life Sciences, University of Glasgow, Glasgow, Scotland, UK. ³Glasgow Imaging Facility, School of Infection and Immunity, College of Medical, Veterinary and Life Sciences, University of Glasgow, Glasgow, Scotland, UK. ✉e-mail: Pablo.Murcia@Glasgow.ac.uk

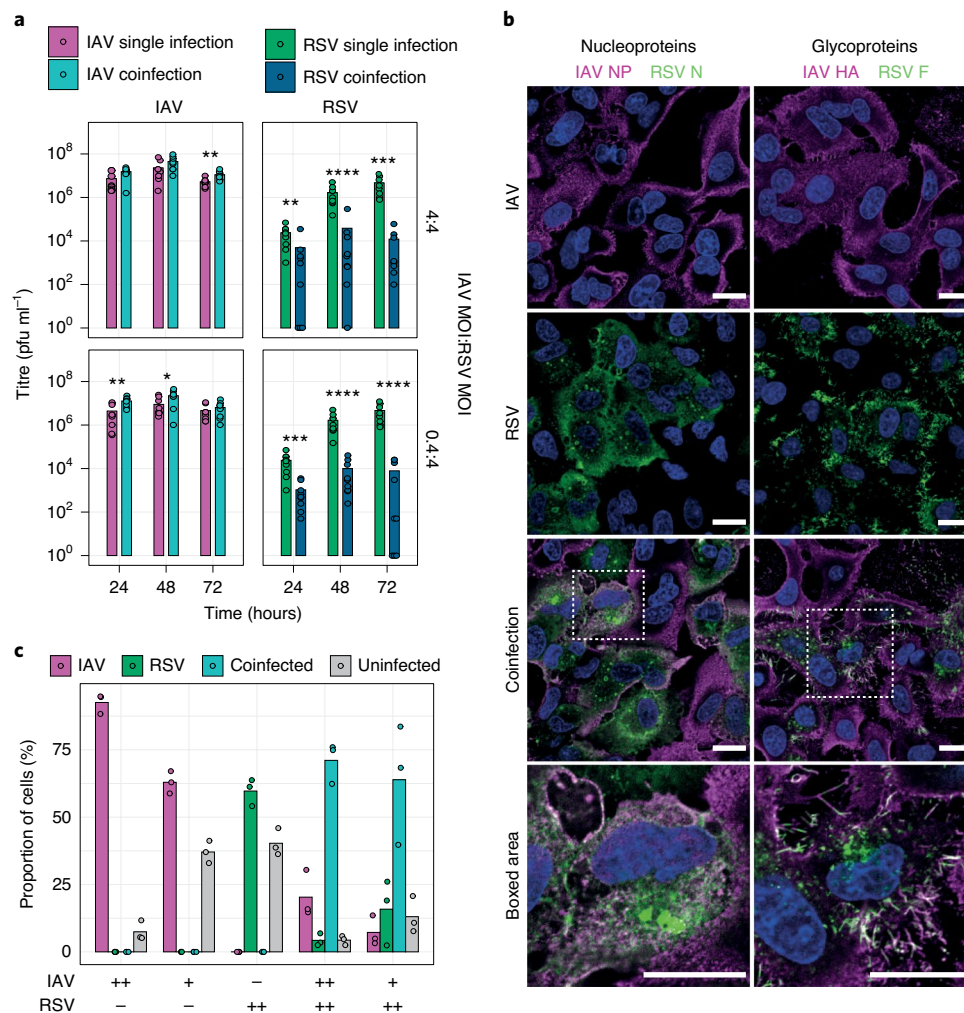


Fig. 1 | Replication kinetics and cellular infection during IAV and RSV coinfections. **a**, Left, IAV replication kinetics in single infection (magenta bars) and mixed infection with RSV (teal bars). Right, RSV replication kinetics in single infection (green bars) and mixed infection with IAV (blue bars). Infections were carried out at equivalent MOI (4:4, top), and with IAV input tenfold less than RSV input (0.4:4, bottom). Data were collected from $n = 3$ biologically independent experiments, each containing $n = 3$ technical replicates, bars represent the mean and data points represent individual replicates. Significance determined by two-tailed Mann–Whitney test, * $P < 0.05$, ** $P < 0.01$, *** $P < 0.001$, **** $P < 0.0001$, non-significance not indicated. Exact P -values as follows: IAV replication, MOI ratio 4:4 (top left) 48 hpi $P = 0.514$, 72 hpi $P = 0.0026$; IAV replication, MOI ratio 0.4:4 (bottom left) 24 hpi $P = 0.0031$, 48 hpi $P = 0.0277$; RSV replication, MOI ratio 4:4 (top right) 24 hpi $P = 0.0060$, 48 hpi $P > 0.0001$, 72 hpi $P = 0.0002$; RSV

replication, MOI ratio 4:4 (bottom right) 24 hpi $P = 0.0002$, 48 hpi $P < 0.0001$, 72 hpi $P < 0.0001$. **b**, Single or coinfecting AS49 cells were fixed at 24 hpi and stained by immunofluorescence for IAV nucleoprotein (magenta) and RSV nucleoprotein (green) (left column) and IAV HA (magenta) and RSV fusion glycoprotein (green) (right column). Nuclei are stained with DAPI (blue). White boxes indicate regions in labelled boxed area, scale bars indicate 20 μm . Images in panel representative of $n = 2$ independent experiments. **c**, Proportion of cells infected with IAV-only (magenta), RSV-only (green), coinfecting (teal) or uninfected (grey) in single-virus infection or mixed at 24 hpi. Panel below plot represents the infection conditions used: - for no virus, ++ for MOI 4 and + for MOI 0.4. Data were collected from $n = 3$ biologically independent experiments, bars represent the mean and data points represent biological replicates.

Results

Viral replication during coinfection of lung cells

Infections were performed at high MOI to facilitate coinfection and recapitulate high MOIs, which are produced in advanced stages of infection (when IAV and RSV foci may come into contact). We compared viral replication in single infections and coinfections. Single IAV infections resulted in robust replication, peaking between 24–48 hours post-infection (hpi). In coinfections, IAV replication was similar to that observed in coinfection or at some timepoints marginally increased (Fig. 1a, top left). As RSV titres peaked in single infections at a later timepoint than IAV (72 hpi, Fig. 1a, top right), further infections were performed to determine optimal conditions for coinfections by using a reduced IAV MOI (tenfold reduction relative to RSV). The reduced IAV input did not affect IAV replication, which still replicated to higher

titres in coinfections (Fig. 1a, bottom left). By contrast, RSV titres were significantly reduced, by over 400-fold at 72 hpi, in the presence of IAV both at equivalent MOI (Fig. 1a, top right) and when IAV MOI was reduced relative to RSV (Fig. 1a, bottom right). These results are consistent with published studies that show that RSV is adversely impacted by coinfection, while IAV replication is not^{17,18}.

Localization of viral proteins during coinfection

To assess if coinfection affected localization of key viral proteins or the proportion of infected cells, single and coinfections were performed as described above and cells were fixed at 24 hpi. Immunofluorescence microscopy revealed that cells infected with either RSV or IAV displayed features typical of the replicative cycle of each virus, such as cytoplasmic inclusion bodies containing RSV nucleoprotein (N), or diffuse IAV

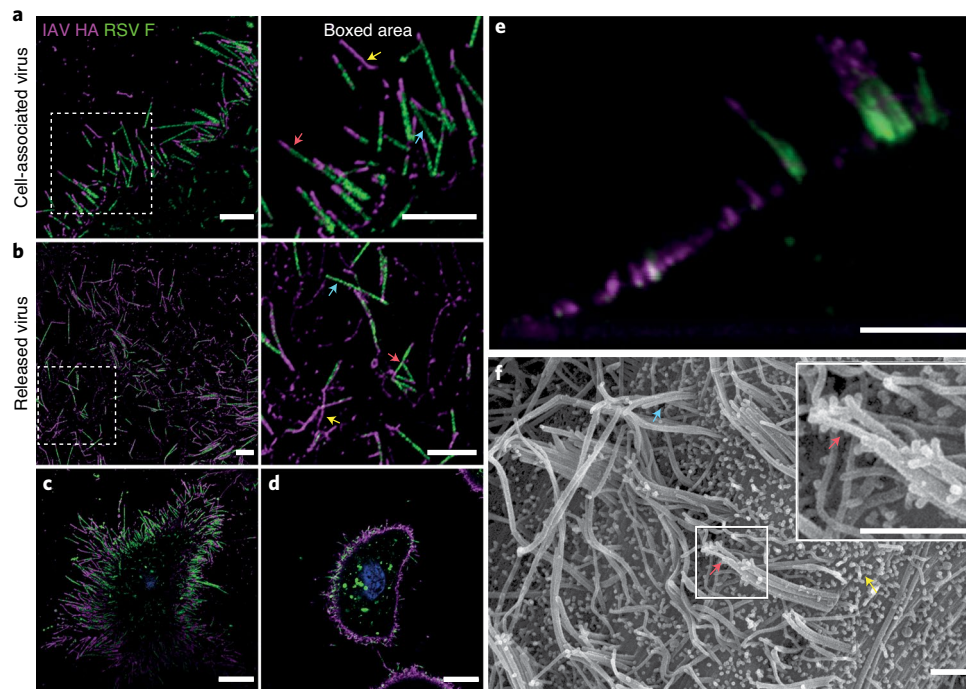


Fig. 2 | Filaments containing both IAV and RSV proteins extend from coinfecting cells. **a, b**, Cell-associated viral filaments positive for IAV HA (magenta on merged image) and RSV F (green on merged image) that are cell associated (**a**) or released (**b**) from coinfecting cells, imaged by super-resolution microscopy. Magnified images of white boxed regions indicate examples of IAV filaments (yellow arrows), RSV filaments (blue arrows) and dual-positive filaments (red arrows). Scale bars indicate 500 nm. **c, d**, Coinfecting cell exhibiting extensive dual-positive filament formation. Cell imaged by confocal microscopy at two

Z-positions: basal side adhered to coverslip (**c**) and through the centre of the cell (**d**). Scale bars indicate 10 μm . **e**, 2D z-plane image reconstructed from a Z-stack of a live cell stained for IAV HA and RSV F, imaged by super-resolution confocal microscopy at 100 nm intervals through the entire cell (16.3 μm). **f**, Scanning electron micrograph of coinfecting cell surface. IAV and RSV particles are indicated by yellow and blue arrows, respectively. Red arrow and magnified region highlight particles that contain structural features of both IAV and RSV. Scale bars indicate 1 μm .

nucleoprotein (NP) staining within the cytoplasm (Fig. 1b, left column). Similar features were observed in coinfecting cells (Fig. 1b, boxed area) suggesting that coinfection did not affect the intracellular localization of viral proteins. We counted the number of infected cells in single infections alongside the number of single-infected and coinfecting cells in the coinfection condition. We observed a high proportion of coinfecting cells at 24 hpi when cells were infected with equivalent amounts of virus as well as when IAV input MOI was reduced tenfold relative to RSV (Fig. 1c), suggesting that superinfection exclusion does not prevent coinfection. Paradoxically, a higher number of RSV-positive cells were detected in coinfections than in RSV single-infected samples, contrasting with the observed reduction in RSV titre in coinfections.

IAV and RSV are enveloped viruses that target lipid rafts for assembly and budding^{19,20}. We therefore stained cells for the major glycoproteins of IAV and RSV: haemagglutinin (HA) and RSV fusion (F), respectively (Fig. 1b, right column) and examined their localization at plasma membranes. IAV HA diffusely coated the plasma membrane of infected cells in both single virus infections and coinfections, while RSV F was localized to regions containing filamentous structures extending from the cell surface, corresponding to budding RSV virions. In coinfecting cells, HA was not excluded from RSV budding sites (Fig. 1b, right column, boxed area).

Filaments containing both IAV and RSV proteins are produced during coinfection

We hypothesized that mixing of glycoproteins within cell surface regions may result in incorporation of both IAV and RSV components to budding viral particles. To test this, we applied super-resolution confocal microscopy to image virions immunolabelled for HA and F at high resolution. We observed dual-positive fluorescence suggesting the presence of budding viral filaments possessing both IAV and

RSV glycoproteins during coinfection (Fig. 2a,b). Strikingly, minimal colocalization between the two glycoproteins was observed. Instead, glycoproteins were incorporated in distinct regions along the filament, with most dual-positive filaments positive for IAV HA at the distal end (Extended Data Fig. 1). Of coinfecting cells, $56 \pm 9.1\%$ (mean \pm SD) displayed cell-associated, dual-positive filaments. Many of these cells showed extensive production of dual-positive filaments, with no obvious indication of cell damage (Fig. 2c,d). We also observed dual-positive filaments distant from coinfecting cells, suggesting they remained intact upon budding (Fig. 2b). Nested among dual-positive filaments (both cell-associated and released), we identified filaments corresponding to IAV and RSV virions (identified by HA or F only staining) (Fig. 2a,b, Extended Data Fig. 1). This indicates that regions in which dual-positive filaments form may contain both IAV and RSV budding sites.

We performed microscopy on live cells to visualize the native organization of the filaments budding from coinfecting cells. Consistent with our previous observations, we detected bundles of filaments protruding from the cell surface that incorporated F along the length of the filament with HA localized at the distal end (Fig. 2e). To obtain better resolution of these budding viruses, we used scanning electron microscopy (SEM). IAV single infection revealed a pleomorphic population of membrane-associated structures consistent with spherical, bacilliform and filamentous particles, whereas RSV single infection resulted in dense clusters of budding RSV filaments (Extended Data Fig. 2). In coinfecting cells we identified RSV-like filaments with structures branching from the distal ends resembling smaller bacilliform IAV-like virions (Fig. 2f).

Ultra-structure of hybrid viral particles determined by cryo-ET
To determine the structural details of IAV or RSV filamentous structures budding from coinfecting cells, we performed cryo-electron tomography (cryo-ET) and observed structures consistent with hybrid viral

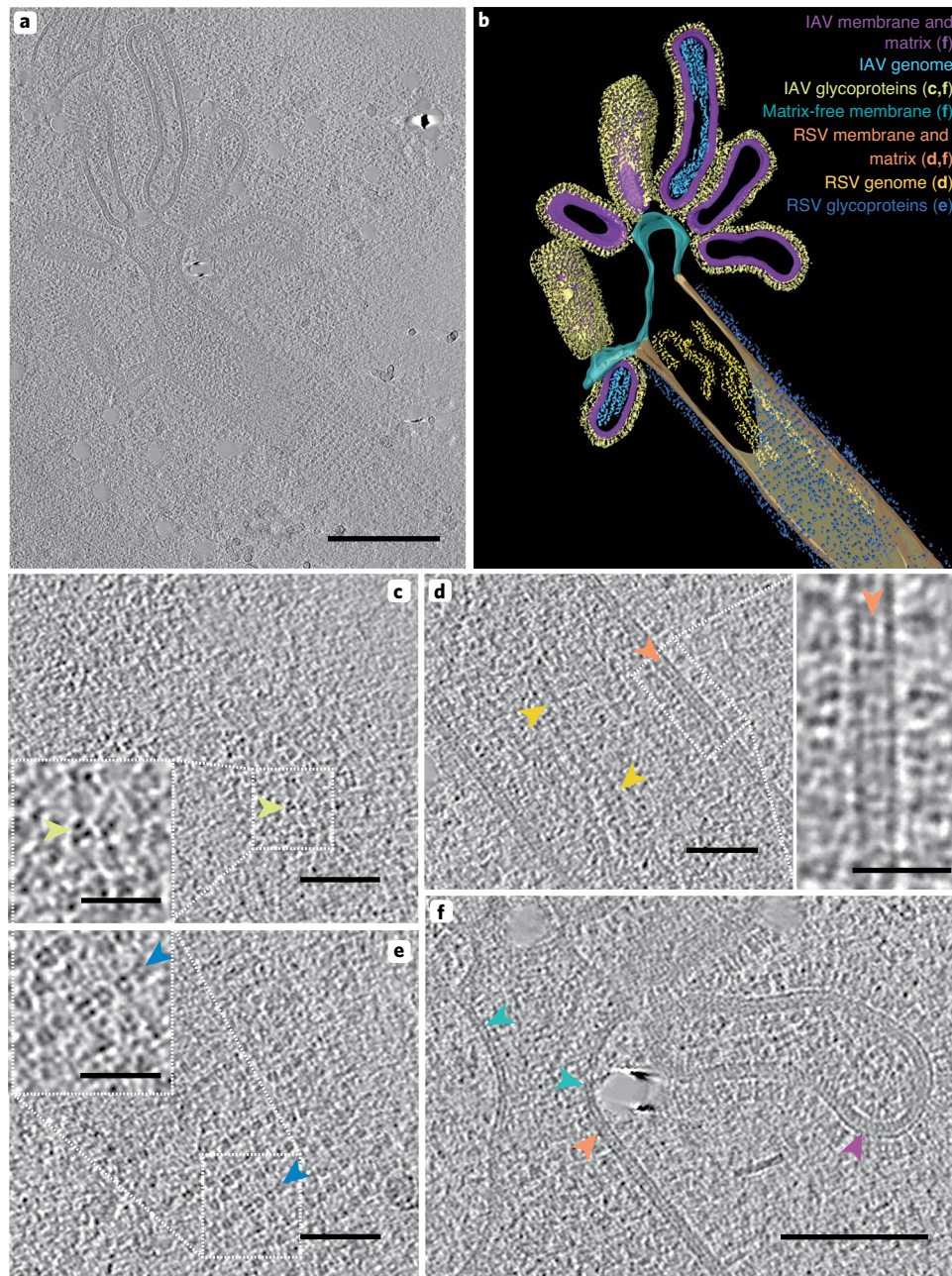


Fig. 3 | Hybrid viral particles contain IAV- and RSV-like structural regions. Viral particles produced from coinfecting A549 cells were frozen at 24 hpi and imaged by cryo-ET. **a**, Cryo-tomogram showing an example of a hybrid viral particle. Particles consisted of an RSV-like region, extending to multiple IAV-like protrusions from the distal end of the filament. Scale bar indicates 200 nm. **b**, Manual segmentation of the cryo-tomogram shown in **a** highlighting examples of key structural features (not all features have been segmented). Coloured labels on figure match coloured segmented volumes and letters denote figure panels in which detailed images of features are shown. **c**, The surface of IAV region shows the ordering of IAV glycoproteins (yellow arrow). Magnified insert shows density associated with HA trimers in a characteristic triangular arrangement, scale bar represents 25 nm. **d**, Cross-section through the RSV region shows RNPs, indicated

by gold arrows. The inset image shows magnified region highlighted by white dashed box, showing the RSV viral envelope associated with the matrix layer (orange arrow). Scale bar in inset image represents 25 nm. **e**, The surface of the RSV region shows the characteristic helical arrangement of glycoproteins into rows (blue arrows). The magnified insert shows circular density corresponding to RSV glycoproteins, scale bar represents 25 nm. **f**, IAV- and RSV-like regions were joined by a continuous membrane bilayer. Coloured arrows indicate presence or absence of matrix layer. Membrane in IAV and RSV region was clearly associated with a matrix layer, indicated by orange and magenta arrows for RSV and IAV respectively, while matrix appeared absent in the adjoining regions (blue arrow). Scale bars indicate 50 nm (**c–e**) or 100 nm (**f**).

particles containing elements of both IAV and RSV. We repeatedly observed two classes of hybrid particle with some virions exhibiting features of both classes: in 11 cryo-tomograms we observed true hybrid virus particles (HVPs, Fig. 3), and in 16 cryo-tomograms we observed pseudotyped viruses (PVs, Extended Data Fig. 3). Pleomorphic IAV particles and RSV filaments were also identified (Supplementary Information, Supplementary Videos 1 and 2).

HVPs exhibited distinct IAV-like and RSV-like structural regions: the wider part of the filament resembled RSV and extended continuously towards the distal end to one or more narrow, IAV-like regions (Fig. 3a,b, Extended Data Fig. 4, Supplementary Videos 1 and 2). Density consistent with both IAV and RSV ribonucleoproteins (RNPs) could be visualized and seemed confined within their respective structural regions of the filaments^{21,22} (Fig. 3a,b,d). Glycoproteins consistent in

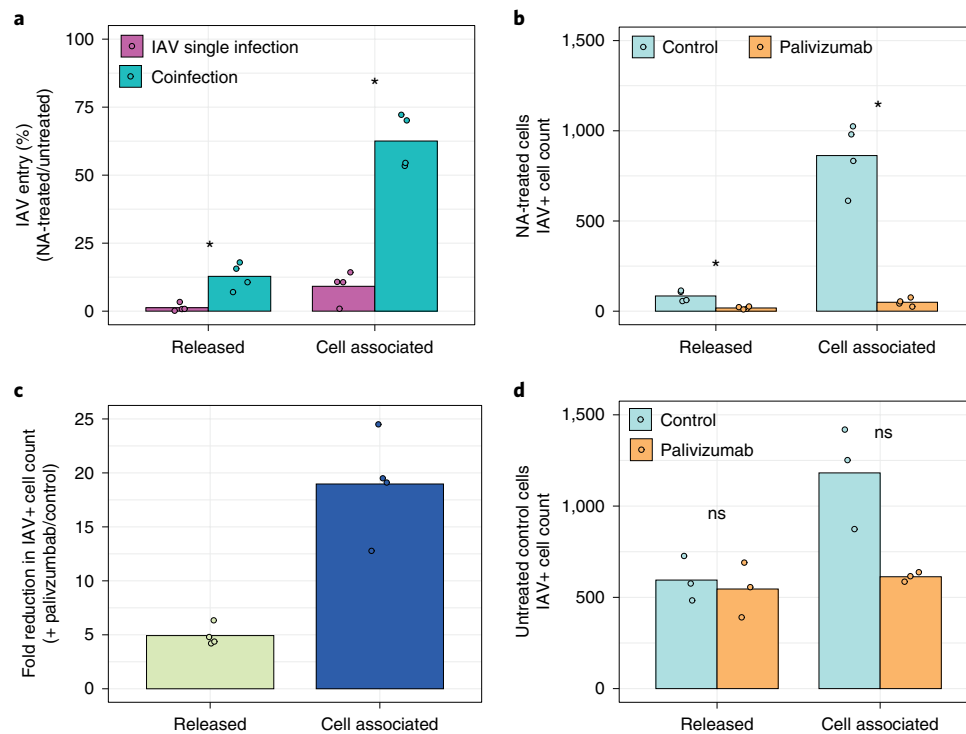


Fig. 4 | Hybrid viruses enable IAV infection in sialic acid-depleted cells.

NA-treated or control A549 cells were infected with virus harvested from coinfection or IAV single infection, fixed and immunostained at 12 hpi and the number of IAV-infected cells was quantified using an automated image-based cell counter. **a**, Ratio of IAV entry into NA-treated cells versus control cells when harvested from single infection (magenta bars) or mixed infection (teal bars). IAV entry to NA-treated cells was calculated as a percentage of the IAV-positive cell count in the matched untreated control. Released $P = 0.0286$; cell associated $P = 0.0286$. **b**, IAV-positive cell count in NA-treated cells infected with virus that was harvested from coinfection and incubated with palivizumab (orange bars) or

a serum free control (cyan bars). Released $P = 0.0286$; cell associated $P = 0.0286$. **c**, Fold change in IAV positive cell counts (as shown in **b**) for released (yellow bar) and cell-associated (navy bar) virus. **d**, IAV-positive cell count in untreated control cells infected with virus that was harvested from coinfection and incubated with palivizumab (orange bars) or a serum-free control (cyan bars). **a–c**, Data were collected from $n = 4$ biologically independent experiments. **d**, Data were collected from $n = 3$ biologically independent experiments. Bars represent the mean and data points represent biological replicates. Statistical significance was determined by a two-tailed Mann–Whitney test. * $P < 0.05$; ns, $P > 0.05$.

size, shape and density with IAV or RSV glycoproteins decorated the respective IAV- or RSV-like regions of the particles (Fig. 3c,e). In some virions, the junction between IAV and RSV regions had a clear lumen (Extended Data Fig. 4c, Supplementary Video 2), while other particles exhibited a much narrower join, with pinching off membranes between IAV and RSV areas (Fig. 3f, Supplementary Video 1, Extended Data Fig. 4a). Matrix layers were observed in IAV and RSV regions but were absent from the membrane bridging the two regions (Fig. 3f).

We also identified virions consistent with RSV filaments containing RSV RNPs that had a different glycoprotein ordering than expected (Extended Data Fig. 3). The glycoproteins differed in shape when compared to those present on RSV virions and had a triangular arrangement which resembled IAV glycoproteins (Extended Data Fig. 3c), rather than ring shaped density more consistent with RSV glycoproteins (Extended Data Fig. 3e). They also lacked the long-range helical ordering typical of RSV glycoproteins (Extended Data Fig. 3c,e)²³. We designated these structures ‘pseudotyped viruses’ (Extended Data Fig. 3a,c,d, Supplementary Video 3). Some HVPs with distinct IAV- and RSV-like structural regions also exhibited pseudotyping within the RSV region (Extended Data Fig. 4a,b). Notably, we did not observe IAV virions or IAV-like regions in hybrid particles that were pseudotyped with RSV glycoproteins.

To quantify differences in glycoprotein arrangement, we determined the inter-spike distance on IAV, RSV and PVs. RSV exhibited a mean (\pm SD) inter-spike spacing of 12.9 (\pm 2.32) nm, while IAV had a spacing of 8.71 (\pm 1.18) nm. PVs had an average spike distance ranging from 8.31–9.56 nm, similar to IAV but significantly different to

RSV ($P < 0.0001$, unpaired t -test; Extended Data Fig. 5). These results confirm that coinfections can result in the formation of two classes of hybrid viral particles structurally distinct from either parental virus.

Antigenicity of hybrid virus particles

As surface glycoproteins determine antigenicity and tropism, and HVPs incorporate glycoproteins of both IAV and RSV, we hypothesized that HVPs would display altered antigenicity. To test this, we first compared the neutralization efficiency of anti-IAV HA antibodies against viruses collected from cells infected with IAV alone, or coinfecting with IAV and RSV. As RSV is predominantly cell-associated, we performed neutralization assays using supernatant and cell-associated fractions (Methods). Viruses were also back-titrated to determine infectious titre of the inoculum (Extended Data Fig. 6a,b). Viruses collected from coinfecting cells displayed reduced IAV neutralization compared to those collected from single IAV infections (Extended Data Fig. 6c). While the observed differences were not statistically significant, the decrease in neutralization efficiency was more marked in the cell-associated fraction of the coinfecting cells (Extended Data Fig. 6c) where only 33% (\pm 27%; mean [\pm SD]) of IAV was neutralized, suggesting that two-thirds of IAV within this fraction was able to evade antibody-mediated neutralization (Extended Data Fig. 6c).

In an analogous experiment, we compared the neutralization efficiency of anti-RSVF antibodies (palivizumab) against viruses collected from cells infected with RSV alone or coinfecting. RSV harvested from both single and mixed infections was efficiently neutralized (Extended Data Fig. 6d). This suggests that, in contrast with IAV, RSV cannot utilize

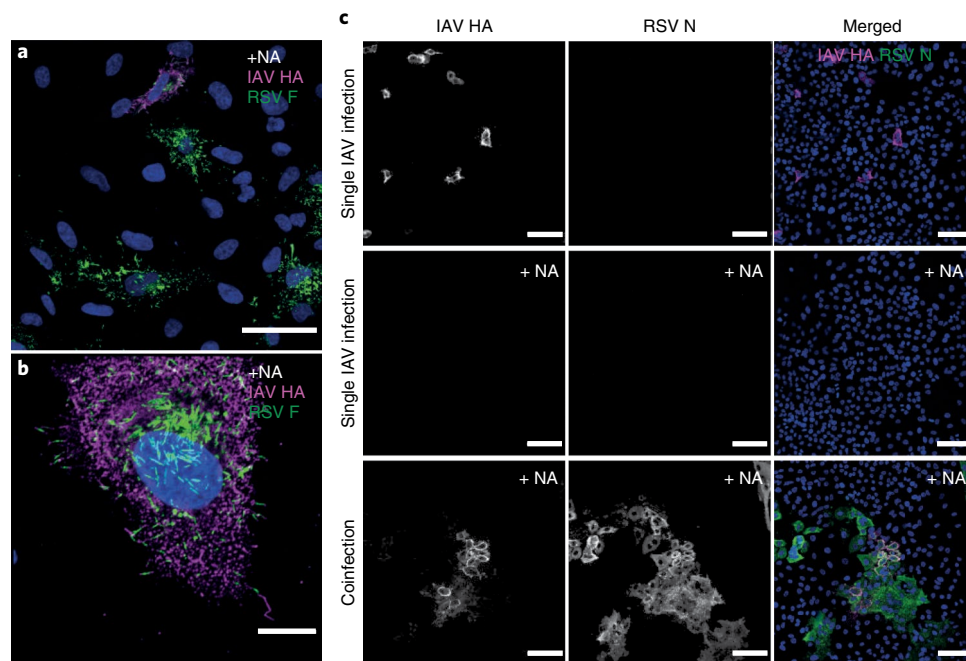


Fig. 5 | Hybrid viral particles enable spread of IAV in a refractory cell population. **a**, A549 cells were infected with cell-associated virus from a coinfection and incubated for 12 hpi, before staining for IAV HA (magenta) and RSV F (green) and imaging by standard confocal microscopy. **b**, Super-resolution confocal imaging of coinfecting cells shows formation of dual-positive filamentous structures, indicating hybrid particle formation is maintained upon passage. **c**, Virus harvested from IAV single infection (top and middle rows) or coinfection (bottom row) was incubated on untreated control wells (top row)

or NA-treated wells (middle and bottom rows) with an overlay for 48 hours. Foci of infection were immunostained for IAV HA (magenta) and RSV N (green) and imaged by confocal microscopy. Infection was observed by IAV from single infection in untreated control cells, but not NA-treated cells. Virus harvested from coinfection formed large foci and IAV foci colocalized with RSV foci. Images shown in **a–c** are representative of $n = 2$ biologically independent experiments. Scale bars: 100 μm (**a**), 1 μm (**b**) and 200 μm (**c**).

IAV glycoproteins to facilitate viral entry. Further, in the context of PVs, RSV infectivity may be determined by the ratio of incorporated IAV and RSV glycoproteins, where fully pseudotyped RSV filaments may be non-infectious, as they are unable to utilize IAV HA.

Receptor tropism of hybrid virus particles

To determine if the incorporation of RSV glycoproteins could result in an expansion of IAV receptor tropism, we treated cells with neuraminidase (NA) to remove sialic acids (the cellular receptor for IAV; Extended Data Fig. 7a). Sialic acid removal was confirmed by lectin staining (Extended Data Fig. 7b). Virus was harvested from IAV or RSV single infections or coinfections as described for neutralization assays and subsequently used to inoculate IAV-receptor-deficient (NA-treated) or control cells (Fig. 4a), as well as being back-titrated to determine the IAV titre in the inoculum (Extended Data Fig. 7c). Cells were fixed at 12 hpi, immunostained for IAV NP or RSV N and infected cells quantified. IAV entry was blocked in NA-treated cells when inoculated with the released virus of single IAV-infected cells, whereas entry of cell-associated IAV collected from single IAV infections was reduced by 90% (Fig. 4a). When NA-treated cells were inoculated with released or cell-associated virus harvested from mixed infections, IAV entry was significantly increased compared to IAV-only infection (Fig. 4a). The increase in IAV entry was higher in the cell-associated fraction, and IAV entry in receptor-deficient cells was restored to 63% ($\pm 10\%$) (mean [\pm SD]) of the level of control cells (Fig. 4a). As RSV does not use sialic acids as receptors, no differences in RSV entry between NA-treated or control cells were detected (Extended Data Fig. 7d).

To determine if extracellular association between free IAV and RSV virions was contributing to IAV entry into NA-treated cells, IAV and RSV were mixed and incubated prior to infecting NA-treated or control cells. No significant differences were observed in IAV or RSV

entry into receptor-deficient cells compared with control cells when the viruses had been pre-mixed (Extended Data Fig. 7e), compared with each virus alone, suggesting that IAV and RSV do not associate upon extracellular mixing or that association does not impact viral entry. Overall, our findings suggest that the increase in IAV entry to sialic acid-deficient cells was a result of hybrid particle formation and indicates that HVPs represent a subpopulation of infectious virus particles with expanded receptor tropism. To determine whether the expansion of IAV tropism was mediated by the RSV F glycoprotein, virus harvested from mixed infections was incubated with palivizumab. We observed a significant reduction in entry of both released and cell-associated IAV into NA-treated cells in the presence of palivizumab (Fig. 4b,c), suggesting that RSV F facilitates IAV infection via hybrid particles that enable IAV to enter cells that would otherwise be refractory to infection. We measured IAV entry into untreated control cells (that is cells with normal expression of sialic acids) in the presence or absence of palivizumab. We observed that in the presence of palivizumab, entry of IAV harvested from the cell-associated fraction of coinfections was reduced by approximately half, compared with the palivizumab-free control (Fig. 4d). This suggests that there is a population of IAV that is dependent on RSV F to gain entry to cells, which in turn suggests that RSV F is the functional glycoprotein of IAV/RSV HVPs.

Infectivity of hybrid viruses

Our cryo-ET data showed that HVPs contain IAV and RSV genomes. To determine if they possess infectivity for both viruses, we infected NA-treated cells with virus harvested from single or mixed infections. At 12 hpi, cells were fixed and stained for IAV HA and RSV F and imaged by confocal microscopy. The presence of coinfecting cells suggested that both genomes were delivered into the cells simultaneously, likely by HVPs (Fig. 5a,b). This conclusion is based on the facts that 12 hours is

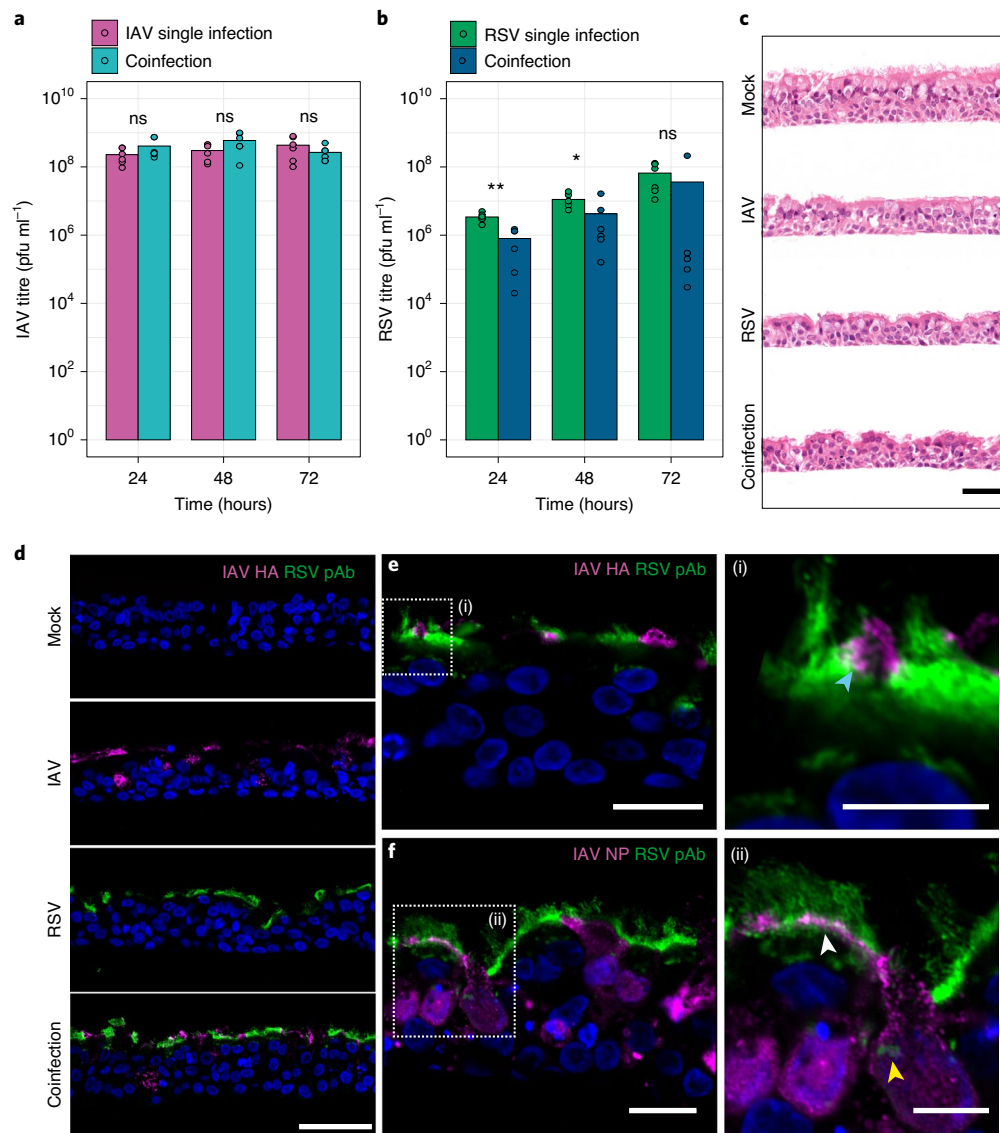


Fig. 6 | Coinfection occurs in primary cells. **a**, IAV replication kinetics in hBEC cultures in single infection (magenta bars) and mixed infection with RSV (teal bars). Infections were carried out in $n = 6$ individual transwells over $n = 3$ biologically independent experiments. Bars represent the mean and data points represent individual replicates. Statistical significance was determined by two-tailed Mann–Whitney test. ns represents $P > 0.05$. **b**, RSV replication kinetics in hBEC cultures in single infection (green bars) and mixed infection with RSV (dark blue bars). Infections were carried out in $n = 6$ individual transwells over $n = 3$ biologically independent experiments. Bars represent the mean and data points represent individual replicates. Statistical significance was determined by two-tailed Mann–Whitney test, 24 hpi $P = 0.0022$, 48 hpi $P = 0.0433$. $**P < 0.01$, $*P < 0.05$, ns $P > 0.05$. **c**, Paraffin embedded sections collected at 24 hpi, stained with haematoxylin and eosin. Scale bar represents 50 μm . **d**, Immunofluorescence showing IAV HA (magenta) and RSV antigen (green)

localization in paraffin embedded sections at 24 hpi. Scale bar represents 50 μm . **e**, Coinfected section imaged by super-resolution confocal microscopy shows localization of IAV HA (magenta) and RSV antigen (green) to the apical surface of epithelial cells. Scale bar represents 20 μm . The magnified area (i) shows the region indicated by the white dashed box, highlighting a coinfecting cell with IAV HA and RSV antigen localized at apical surface (blue arrow), scale bar represents 5 μm . **f**, Localization of IAV NP (magenta) and RSV antigen (green) within coinfecting cells. Scale bar represents 20 μm . The magnified area (ii) shows the region indicated by the white dashed box highlighting IAV NP and RSV antigen within the cytoplasm, where RSV inclusion bodies can be observed (yellow arrow), and at the apical surface of coinfecting cells (white arrow). Scale bar indicates 10 μm . Images in (c–f) representative on $n = 3$ biologically independent experiments.

not a sufficiently long time to allow extensive cell-to-cell spread by IAV and RSV that may result in coinfection, and because the probability of coinfection by chance was low as the MOI for each virus was approximately 0.01 (based on back-titrations of harvested virus). Examination of coinfecting cells using super-resolution microscopy revealed viral IAV HA and RSV F double-positive filaments (Fig. 5b), suggesting that the HVPs can be maintained over virus passage. To establish if HVPs could spread IAV from cell to cell within a population of cells refractory to IAV infection, we infected NA-treated or control cells with virus harvested from IAV single infections or from the cell-associated fraction of mixed

infections (the fraction with enriched HVPs). We then applied an overlay to prevent virion diffusion and incubated the cells for 48 hours. As expected, in single IAV infections, abundant IAV-positive cells were observed in non-treated cells (Fig. 5c, top row). In the NA-treated cells, no infection by IAV from single infections was observed (Fig. 5c, middle row), whereas IAV foci consisting of multiple distinct infected cells were observed in NA-treated cells infected with virus from mixed infections (Fig. 5c, bottom row). Notably, IAV-positive foci colocalized with RSV-positive foci (Fig. 5c, bottom row). These results suggest that HVPs can mediate the spread of IAV within a refractory cell population.

Cellular coinfection occurs in primary differentiated airway cells

To determine the potential for HVP formation in a more biologically relevant system, we coinfecting differentiated primary human bronchial epithelial cells (hBECs). We observed no difference in IAV replication kinetics between single-infected and coinfecting cultures (Fig. 6a). In coinfections, RSV titres were variable, but the average titres over experimental replicates were lower than in single infections (Fig. 6b). Trends in replication kinetics between single and mixed infections matched the trends observed in A549 cells, providing confidence that viral interactions are conserved between the two systems. To examine the spread of IAV and RSV in hBECs, we fixed and paraffin-embedded infected or mock-infected cultures (culture morphologies shown in Fig. 6c), and performed immunostaining using antibodies targeting IAV HA, IAV NP and a polyclonal antibody raised against the whole RSV virion. We observed diffuse staining for IAV HA and RSV across the apical layer of cells in single infections, whereas in coinfecting cultures there was a high degree of individual cells infected by each virus as well as evidence of coinfecting cells (Fig. 6d). Analysis of individual coinfecting cells revealed dual staining for both IAV and RSV antigens both at the apical surface of coinfecting cells and within the cytoplasm (Fig. 6e,f), providing an opportunity for interactions between IAV and RSV and the formation of HVPs.

Discussion

Respiratory viruses share a common tropism for the human respiratory tract and cause significant disease burden. Although there is increasing evidence that interactions among viruses play an important role in virus dynamics and transmission, most of what is known about virus biology and pathogenesis is based on a tractable but reductionist research approach, whereby each virus is studied in isolation. Recent work provided evidence that interactions among respiratory viruses occur and have measurable outcomes at multiple levels, from populations, to individuals and tissues^{24–28}. However, studies characterizing direct virus–virus interactions within cells are scarce. Here we report previously unknown interactions between IAV and RSV, two clinically important respiratory viruses that belong to different taxonomical families.

We show that in coinfections, IAV replicates to equivalent or marginally higher titres compared to single IAV infections, whereas RSV replication is reduced. The consistency in IAV replication kinetics in the presence or absence of RSV contrasts with the inhibition of IAV replication in coinfections with rhinovirus²⁶. This indicates that the consequences of coinfections are highly dependent on the viruses involved as they trigger virus-specific cellular responses.

We also show compelling evidence that coinfections can generate infectious HVPs composed of structural, genomic and functional components of both parental viruses. As HVPs can evade IAV-targeted neutralization and infect cells lacking IAV receptors suggests that coinfections can generate viruses with altered antigenicity and expanded tropism. Using palivizumab, we showed that RSV F mediates HVP entry, indicating that in the context of a hybrid particle, IAV can use the glycoprotein of an unrelated virus as its functional envelope protein. This property may facilitate within-host dissemination to areas of the respiratory tract that are refractory to infection by one of the parental viruses, which is likely to impact pathogenesis and disease outcome. For example, IAV predominantly infects the upper and middle respiratory tract causing uncomplicated influenza, while RSV spreads more readily to the middle and lower respiratory tract (LRT)^{29,30}. HVPs could enable IAV to escape mucosal antibodies while spreading to the LRT, with subsequent potential complications, including viral pneumonia³⁰. In addition, as IAVs exhibit high mutation rates, LRT infections by HVPs might favour the selection of IAVs with increased tropism for the LRT and, therefore, result in selection of more pathogenic viruses.

In recent years, a conceptual framework that incorporates social evolution theory has been developed to explain how virus–virus interactions can have a substantial effect on virus function and fitness³¹.

We show that HVP formation is maintained over multiple rounds of infection, and that HVPs facilitate the spread of IAV within a population of refractory cells. This observation aligns with the concept that, like other pathogens and organisms, viruses can engage in social-like traits that are beneficial to virus fitness and function.

Using a lung-derived human cell line, we show that the generation of HVPs by coinfection is biologically feasible. The fact that IAV and RSV cocirculate in winter in the same populations¹, have a shared tropism for ciliated epithelial cells^{32,33}, bud from the apical cellular surface^{22,33,34} and coinfect cells within the respiratory epithelium (this work) suggest that HVPs have the potential to be generated in vivo. The likelihood of a cell becoming coinfecting during natural infection remains unknown but will vary depending on the timing of infection and the localization of infectious foci within the respiratory tract. Estimates of viral bursts show that as viral load increases, the effective MOI to susceptible cells surrounding an infectious focus increases³⁵, enhancing the probability of cellular coinfection and therefore the potential generation of HVPs.

The formation of HVPs raises questions about fundamental rules that govern viral assembly and budding. These processes, which are thought to be highly regulated, involve selective recruitment, trafficking^{36,37} and multimerization of viral proteins^{19,38–40} within specific compartments of the cell. While we described the formation of HVPs as a consequence of coinfection by IAV and RSV, we hypothesize that coinfections involving other pleomorphic enveloped viruses are also likely to generate HVPs. However, we posit that formation of infectious HVPs requires more than structural compatibility, and includes similar tropism, absence of superinfection exclusion or interference, as well as seasonal and geographical co-circulation. RSV is a pleomorphic enveloped virus with a broad tropism for different regions of the respiratory tract and is frequently observed in co-infections in winter^{41–43}, therefore RSV is a good candidate to form HVPs with other respiratory viruses. This might explain some of the mechanisms that lead to viral pneumonia⁴⁴.

One limitation of this study is that experiments were carried out in cell culture systems. While primary differentiated human airway cells provide the closest human-derived model of the upper respiratory tract available, they cannot fully capture the spatial and physiological complexity of the whole respiratory tract. Therefore, further in vivo studies are required to determine the frequency of coinfection within respiratory tissues and the potential for HVP formation. Additionally, further studies will be required to address which virus combinations can generate infectious HVPs; which viral properties favour their formation; and how they impact on pathogenesis and virus transmission.

Methods

Cells

Human lung adenocarcinoma cells (A549; American Type Culture Collection (ATCC), CCL-185), Madin–Darby canine kidney (MDCK) cells (ATCC, CCL-34) and HEp-2 (ATCC, CCL-23) cells were cultured in Dulbecco's Minimum Essential Media (DMEM), high glucose, GlutaMAX supplemented with 10% fetal bovine serum (FBS). HEp-2 cells were not authenticated before use in this study as these were used only for the propagation and titration of RSV, not coinfection experiments.

The hBECs were cultured and differentiated at the air–liquid interface as described previously²⁴. Briefly, hBECs (Epithelix) were cultured in Epithelix human airway epithelial cell medium (Epithelix; EP09AM) 37 °C, 5% CO₂ in a humidified incubator. Cells were cultured in tissue culture flasks until 80% confluent. After this point, cells were trypsinized and seeded at 2×10^4 cells per transwell onto transwell inserts for 24-well plate with 0.4 µm pore size with a pore density of 1.6×10^6 pores per cm² (Falcon, 734–0036). When cells were fully confluent on transwell membranes, apical media was removed to initiate air–liquid interface (ALI). Basal media was replaced with Pneumacult-ALI media (STEMCELL Technologies, 05001). Basal media was replenished every 2–3 days. When cultures began producing mucus (approximately

20 days post ALI initiation), the apical surface of cultures was washed twice weekly with serum free DMEM.

Viruses

H1N1 influenza A/Puerto Rico/8/34 was rescued as previously described⁴⁵ and virus stocks were grown in MDCK cells. RSV strain A2 (ATCC, VR-1540) was grown in HEp-2 cells.

Antibodies

The following primary antibodies were used at optimized concentrations: RSV fusion glycoprotein (Abcam, UK, AB24011, 1/1,000), RSV nucleoprotein (Abcam, UK, AB22501, 1/1,500), antisera to influenza A H1 (A/Puerto Rico/8/34, 1/1,000; NIBSC, UK, 03/242), influenza A virus nucleoprotein (European Veterinary Society, EVS238, 1/1,000), mouse monoclonal anti-IAV (A/Puerto Rico/8/34) HA (Sinobiological, 11684-MM03, 1/500), polyclonal anti-IAV (A/Puerto Rico/8/34) nucleoprotein kindly provided by P. Digard, goat polyclonal anti-RSV (Abcam, AB20745, 1/500). Secondary antibodies: rabbit anti-mouse IgG alexafluor 488 conjugate (Sigma-Aldrich, USA, SAB4600056, 1/1,000), donkey anti-mouse 594 conjugate (Abcam, UK, ab150108, 1/1,000) donkey anti-sheep alexafluor 594 conjugate (Thermo Fisher Scientific, USA, A-11016, 1/1,000), goat anti-rabbit alexafluor 488 (Invitrogen, A11034).

Virus growth curves

A549 cells were infected with IAV, RSV or synchronously infected with a mixed inoculum of IAV and RSV, diluted in DMEM, with 2% FBS and 1 $\mu\text{g ml}^{-1}$ trypsin TPCK. Infections were carried out with RSV at a multiplicity of infection (MOI) of 4 and IAV at an MOI of 4 or 0.4. A549 cells were inoculated in 48-well plates and incubated at 37 °C, 5% CO₂ for 90 minutes, before the inoculum was removed and replaced with DMEM, with 2% FBS and 1 $\mu\text{g ml}^{-1}$ trypsin TPCK. Cells were incubated at 37 °C, 5% CO₂ and supernatant from each infection was collected at 24, 48 and 72 hours post-infection and stored at -80 °C prior to titration by plaque assay.

The hBEC cultures were infected no earlier than 35 days after ALI initiation. The apical surface of cultures was washed with DMEM 24 hours prior to infection by applying pre-warmed DMEM to the apical surface of cultures and incubating at 37 °C, 5% CO₂ in a humidified incubator for 20 minutes, followed by removal. This washing step was repeated immediately before infection. Inoculum containing 10⁵ pfu of IAV, RSV or a mixed inoculum of both viruses (10⁵ pfu of each virus) was prepared in DMEM. Cultures were incubated with inoculum for 2 hours at 37 °C 5% CO₂, after which the inoculum was removed and cultures were washed once with DMEM as described. Inoculum was back titrated by plaque assay to confirm virus input and served as the zero hours timepoint for growth curves. Two cultures were infected per infection condition and experimental timepoint. Samples were collected from the apical surface of cultures at 24, 48 and 72 hpi, by incubating with DMEM for 30 minutes. Samples were then removed and stored at -80 °C, prior to titration by IAV or RSV plaque assay. Transwells were fixed with 4% formaldehyde for 1 hour. After fixation, hBEC cultures were embedded in paraffin blocks, cut to sections of 2–3 μm thickness and mounted on glass slides. Sections were stained with haematoxylin and eosin to determine morphology.

Infectious titre was determined by plaque assay in MDCK cells or HEp-2 cells for IAV and RSV, respectively. Validation was carried out prior to these experiments to ensure specific detection of IAV or RSV plaques in the respective cell type. While IAV and RSV are capable of infecting both cell lines, each cell line is only permissive to plaque formation by one virus, that is, IAV forms plaques in MDCK but not HEp-2 cells, while RSV forms plaques in HEp-2 but not MDCK cells. Viruses were titrated in tenfold serial dilutions in duplicate and incubated on confluent cell monolayers for 90 minutes. For IAV plaque assays, overlay containing DMEM, 1 $\mu\text{g ml}^{-1}$ trypsin TPCK and 0.6% Avicel was used and plates were incubated at 37 °C, 5% CO₂ for 48 hours.

For RSV plaque assays, overlay containing DMEM, 5% FBS and 0.6% Avicel was applied and plates were incubated at 37 °C, 5% CO₂ for 4–5 days. Plates were then fixed with 4% formaldehyde in phosphate buffered solution (PBS) and stained with 0.1% Coomassie Brilliant Blue. Plaques were counted and titre determined as plaque forming units per ml (pfu ml⁻¹). Experiments were carried out in technical ($n = 3$) and biological triplicate ($n = 3$ independent experiments).

Immunofluorescence and confocal microscopy

Cells were seeded at 2 × 10⁵ cells ml⁻¹ on 13 mm glass coverslips or 35 mm glass bottom dishes (MATTEK Corporation Inc, USA) prior to infection. Infections were incubated for 24 hours prior to fixation with 4% formaldehyde in PBS. Fixed cells were permeabilized with 0.1% triton X100 for 10 minutes at room temperature. Samples were blocked with 1% bovine serum albumin (BSA) in PBS for 30 minutes. Primary and secondary antibodies were diluted in 1% BSA in PBS and incubated for 60 minutes at room temperature, followed by four washes with PBS. Coverslips were mounted with Prolong Gold mounting media with DAPI (4',6'-diamidino-2-phenylindole; Invitrogen, USA, P36392), and samples in dishes were stained with 2 $\mu\text{g ml}^{-1}$ Hoescht 33342 solution for 10 minutes. For combining mouse primary antibodies, samples were blocked in rabbit serum (Gentex, USA, GTX73221), then stained with primary antibody and rabbit anti-mouse secondary antibody, followed by secondary blocking in donkey serum (Gentex, USA, GTX73205), then stained with primary antibody and donkey anti-mouse secondary antibody. For live-cell imaging, cells were incubated with 2 $\mu\text{g ml}^{-1}$ Hoescht 33342 solution in cell culture media, for 30 minutes at 37 °C. Cells were then washed with cold PBS, followed by incubation with primary antibody diluted in 2% BSA in PBS for 5 minutes on ice. Cells were washed three times with cold PBS and incubated with secondary antibody diluted in 2% BSA in PBS for 5 minutes on ice. Cells were stored in PBS and imaged immediately following staining.

For immunofluorescence staining of culture sections, sections were dewaxed by heating in an oven at 60 °C for 1 hour. Next, slides were washed four times with xylene, each for 10 minutes. Following this, sections were rehydrated via washes with 1:1 (v/v) xylene:isopropanol mixture, then 100%, 90%, 70% and 50% isopropyl alcohol solution each for five minutes. Sections were washed thoroughly with distilled H₂O and PBS. For antigen retrieval, sections were treated with proteinase K solution (Dako, S3020) for 15 minutes.

Sections were mounted into humid chambers for immunostaining. Sections were permeabilized with 1% triton X100 for 10 minutes, followed by three washes with PBS. Sections were blocked with 2% BSA in PBS for 30 minutes at room temperature. Primary antibodies were diluted in 2% BSA solution and applied to sections for two hours at room temperature, followed by washing with PBS. Secondary antibodies were diluted in 2% BSA solution and applied to sections for 1 hour in the dark at room temperature, followed washing with PBS and distilled H₂O. Slides were mounted with Prolong Gold mounting media containing DAPI (Invitrogen, P36392).

Confocal microscopy was carried out using Zeiss LSM880 AxioObserver microscope (ZEISS, Germany). Standard images were collected using GaAsP detector with 405 nm, 488 nm and 598 nm excitation lasers, using 40×/1.4 or 63×/1.4 plan-apochromat oil DIC M27 objectives. Super-resolution imaging was collected using the Airyscan detector with 405 nm, 488 nm and 594 nm excitation lasers, using plan-apochromat 63×/1.4 oil DIC M27 objective. Z-stacks were collected using a z-interval of 100 nm. For determining proportions of infection and focus assay on NA-treated cells, fields of view were imaged using 3 × 3 tile scans at 40×/1.4 oil DIC M27 objective. Image processing and analysis was carried out in ImageJ software (v2.0.0-rc-56/1.52g; NIH, USA) and Zeiss Zen lite (Blue edition) version 2.6. Single or coinfecting cells were counted manually, using cell counter plugin on ImageJ. Experiments were carried out in technical ($n = 3$) and biological triplicate ($n = 3$ independent experiments).

Scanning electron microscopy

Cells were seeded at 2×10^5 cells ml^{-1} on 13 mm glass coverslips prior to infection at MOI of 4 with IAV, RSV or coinfection for 24 hours. Cells were fixed with 1.5% glutaraldehyde in 0.1 M sodium cacodylate (SC) buffer for 1 hour and washed three times for 5 minutes each with 0.1 M SC buffer before incubation with 1% osmium tetroxide for 1 hour. Samples were then stained with aqueous 0.5% uranyl acetate for 1 h and further dehydrated through an ethanol series and subjected to critical point drying using an Autosamdri-815 Critical Point Dryer (Tousimis, USA) before mounting and coating in 20 nm gold/palladium using a Quorum Q150T ES high vacuum coating system (Quorum Technologies, UK). Images were collected using JEOL IT100 SEM at 20 kV, with InTouch Scope software, version 1.05 (JEOL USA Inc, USA). Infections and imaging were carried out in two independent experiments, with duplicate samples per experiment.

Cryo-electron tomography and computational analysis

Cells were seeded at 2×10^4 cells ml^{-1} on laminin-coated (Roche) 200-mesh gold R2/2 London finder Quantifoil grids (Electron Microscopy Sciences) in 35 mm glass bottom dishes (MATTEK Corporation Inc, USA). Cells were infected with IAV MOI1 and RSV MOI4 and incubated for 24 hours at 37 °C. Cryo-ET imaging experiments of coinfecting cells were carried out in three independent experiments, with duplicate grids imaged per experiment. Immediately before plunge-freezing 3 μl colloidal solution of 20 nm gold fiducials (Sigma-Aldrich) pretreated with BSA was added to each grid. The gold served as fiducial markers for cryo-tomogram reconstruction. Grids were blotted from the backside of the grid and plunge-frozen into liquid ethane using the FEI Vitrobot Mark IV (Thermo Fisher Scientific, USA) or Leica EM GP 2 (Leica Microsystems, Germany). Plunge-frozen grids were subsequently loaded into a JEOL CRYO ARM 300 (JEOL Ltd, Japan) equipped with an energy-filter and DE64 detector (Direct Electron, USA). To identify the presence of virus budding sites near electron transparent cellular edges low-magnification grid maps were generated using serialEM⁴⁶. Next, polygon maps at 3,000 \times magnification were collected at areas of interest and virus budding sites were identified. Tilt-series of virus budding sites were then recorded using SerialEM at either 30,000 \times (1.921 Å per pixel) or 50,000 \times (1.499 Å per pixel) magnification. Each tilt-series was collected from -60° to $+60^\circ$ at an increment of 2° or 3° at 5- to 8- μm underfocus (30,000 \times) and 2- to 5- μm underfocus (50,000 \times). The cumulative dose of one tilt-series was between 80 and 120 $\text{e}^- \text{Å}^{-2}$. Tilt-series were collected using a dose-symmetric scheme starting at 0° implemented in SerialEM⁴⁷ and were collected in 'movie mode'. For the 30,000 \times magnification tilt-series movie frames were aligned using alignframes module in IMOD⁴⁶. For the 50,000 \times magnification tilt-series movie frames were aligned using MotionCor2 with 6 by 6 patches⁴⁸. Once tilt-series sub-frames were aligned and binned eightfold, they were reconstructed into 3D tomograms using weighted back projection with IMOD. To aid interpretation and visualization, noise reduction was applied using Topaz⁴⁹. Figures and supplementary videos were prepared using IMOD, ImageJ and Quicktime. Segmentation and isosurface rendering were performed manually using the thresholding tool in Amira (Thermo Fisher Scientific, USA).

Glycoprotein-distance was measured and calculated using the imodinfo module in IMOD. Denoised tomograms were averaged between 5–10 slices to improve contrast and glycoproteins were viewed from top down. Distances were measured between the centres of pairs of adjacent glycoproteins. For IAV and RSV controls, spike measurements were collected from 11 individual tomograms for each virus ($n = 326$ for IAV, $n = 236$ for RSV). For pseudotyped virus, spike measurements were collected from each particle, from four individual tomograms ($n = 50$ measurements per tomogram).

Neutralization assays

A549 cells were seeded at 1×10^5 cells per well in 24-well plates prior to infection with IAV MOI1, RSV MOI4 or mixed infection. Infected cells

were incubated for 24 hours before released virus was harvested from supernatant and cell associated virus was collected by scraping and vortexing infected cells. Virus stocks were back titrated in MDCK or HEp-2 cells to determine pfu per well in the neutralization assays. For IAV neutralization assay, IAV from single infection or mixed infection was incubated with polyclonal anti-serum targeting A/Puerto Rico/8/34 H1 (NIBSC, UK, 03/242) at 1/200 dilution in DMEM or a serum-free control. For the RSV neutralization assay, RSV from single infection or mixed infection was incubated with Palivizumab (Evidentec, Germany) at 10 μg per well concentration diluted in DMEM, or a serum-free control. Virus (neat or at a 1/10 dilution in DMEM) was incubated with serum for 1 hour at 37 °C before transfer to A549 cells that had been seeded at 1×10^4 cells per well in 96-well plates 48 hours prior to infection. Infections were incubated for 12 hours at 37 °C and following this, cells were fixed in 4% formaldehyde. Plates were immunofluorescence stained for IAV or RSV nucleoprotein and infected cells were quantified using the Celigo automated cytometer (Nexcelom Bioscience, USA), using two target expression analysis. Neutralization was calculated from the positive cell count in each technical replicate of the serum containing wells as a percentage of the average positive cell count in the serum-free control. Experiments were carried out in biological triplicate ($n = 3$ independent experiments).

Neuraminidase assay

To prepare fresh virus stocks for the NA assay, A549 cells were seeded at 1×10^5 cells per well in 24-well plates prior to infection with IAV MOI1, RSV MOI4 or mixed infection. Infected cells were incubated for 24 hours before released virus was harvested from supernatant and cell-associated virus was collected by scraping and vortexing infected cells. Virus stocks were back titrated in MDCK or HEp-2 cells to determine pfu per well in the neutralization assays. For the NA assay, cells were seeded at 1×10^4 cells per well in 96-well plates, prior to treatment with $1 \text{mU } \mu\text{l}^{-1}$ NA from clostridium perfringens (Sigma-Aldrich, USA, N2876) for 2 hours. To confirm removal of sialic acids, NA treated and control cells were stained with biotinylated Maackia Amurensis Lectin II (MAL II; Vector Laboratories, UK, B-1265-1), followed by fluorescein conjugated streptavidin (Vector Laboratories, UK, SA-5001-1) or Erythrina Cristagalli Lectin conjugated to fluorescein (Vector Laboratories, UK, FL-1141-5). Neat virus stocks were transferred directly onto NA treated or untreated cells in 96-well plates or on 13 mm glass coverslips and incubated for 12 hours. Virus harvested from coinfection was also incubated with 10 μg per well palivizumab for 1 hour at 37 °C, before transfer to NA-treated or untreated control wells and incubated for 12 hours. Cells were fixed and 96-well plates stained for IAV or RSV nucleoprotein, followed by rabbit anti-mouse 488 (Sigma Aldrich, USA, SABA4600056) secondary antibody. Infected cells were counted using Celigo automated cytometer (Nexcelom Bioscience, USA), using two target expression analysis. Viral entry ratio was calculated from the positive cell count in each technical replicate of the NA-treated wells as a percentage of the average positive cell count in the untreated control wells. Fixed coverslips were immunostained for IAV HA or RSV F and imaged by confocal microscopy using Zeiss LSM880 with or without Airyscan detector. Experiments were carried out in biological triplicate ($n = 3$ independent experiments).

For the focus assay, cells were seeded onto 13 mm glass coverslips at 1×10^5 cells per well. Cells were treated with $1 \text{mU } \mu\text{l}^{-1}$ NA for 2 hours, before infection with fresh virus stocks harvested from IAV single infection or coinfection or infection of untreated control cells. Infections were overlaid with DMEM containing 0.6% Avicel, 2% FBS and $1 \mu\text{g ml}^{-1}$ trypsin TPCK and incubated at 37 °C for 48 hours. Following this, coverslips were fixed and immunostained for RSV N and IAV HA. Samples were imaged by confocal microscopy using Zeiss LSM880.

Statistical analysis and data visualization

Statistical tests were carried out using Graphpad Prism, version 9.1.0. No assumptions about data normality were made and a two-tailed

Mann–Whitney test was used to determine statistical significance in growth kinetic experiments, neutralization assays and NA assays. For inter-spike measurements on tomograms, normal distribution was tested using the Shapiro–Wilk test and statistical difference between groups was determined by a two-tailed unpaired *t*-test. Data were visualized with RStudio version 1.3.1056⁵⁰ using GGPlot2 package⁵¹. Statistical significance is indicated in figures as ns $P > 0.05$, * $P < 0.05$, ** $P < 0.01$, *** $P < 0.001$, **** $P < 0.0001$.

Reporting summary

Further information on research design is available in the Nature Research Reporting Summary linked to this article.

Data availability

Representative tomograms of the chimeric virus particles described in this paper have been deposited in the Electron Microscopy Data Bank (www.ebi.ac.uk/emdb) under accession codes EMD-13228 and EMD-13229. Source data are provided with this paper.

References

- Nickbakhsh, S. et al. Extensive multiplex PCR diagnostics reveal new insights into the epidemiology of viral respiratory infections. *Epidemiol. Infect.* **144**, 2064–2076 (2016).
- Franz, A. et al. Correlation of viral load of respiratory pathogens and co-infections with disease severity in children hospitalized for lower respiratory tract infection. *J. Clin. Virol.* **48**, 239–245 (2010).
- Goka, E. A., Vallely, P. J., Mutton, K. J. & Klapper, P. E. Single and multiple respiratory virus infections and severity of respiratory disease: a systematic review. *Paediatr. Respir. Rev.* **15**, 363–370 (2014).
- Scotta, M. C. et al. Respiratory viral coinfection and disease severity in children: A systematic review and meta-analysis. *J. Clin. Virol.* **80**, 45–56 (2016).
- Asner, S. A. et al. Clinical disease severity of respiratory viral co-infection versus single viral infection: a systematic review and meta-analysis. *PLoS ONE* **9**, e99392 (2014).
- Asner, S. A., Rose, W., Petrich, A., Richardson, S. & Tran, D. J. Is virus coinfection a predictor of severity in children with viral respiratory infections? *Clin. Microbiol. Infect.* **21**, 264 (2015).
- Echenique, I. A. et al. Clinical characteristics and outcomes in hospitalized patients with respiratory viral co-infection during the 2009 H1N1 influenza pandemic. *PLoS ONE* **8**, e60845 (2013).
- Zavada, J. The pseudotypic paradox. *J. Gen. Virol.* **63**, 15–24 (1982).
- Duverge, A. & Negroni, M. Pseudotyping lentiviral vectors: When the clothes make the virus. *Viruses* **12**, 1311 (2020).
- Akina, R. K. et al. High-efficiency gene transfer into CD34+ cells with a human immunodeficiency virus type 1-based retroviral vector pseudotyped with vesicular stomatitis virus envelope glycoprotein. *J. Virol.* **70**, 2581–2585 (1996).
- Boni, M. F. et al. Evolutionary origins of the SARS-CoV-2 sarbecovirus lineage responsible for the COVID-19 pandemic. *Nat. Microbiol.* **5**, 1408–1417 (2020).
- Smith, G. J. et al. Origins and evolutionary genomics of the 2009 swine-origin H1N1 influenza A epidemic. *Nature* **459**, 1122–1125 (2009).
- Lafond, K. E. et al. Global burden of influenza-associated lower respiratory tract infections and hospitalizations among adults: A systematic review and meta-analysis. *PLoS Med.* **18**, e1003550 (2021).
- Nair, H. et al. Global burden of acute lower respiratory infections due to respiratory syncytial virus in young children: a systematic review and meta-analysis. *Lancet* **375**, 1545–1555 (2010).
- Shi, T. et al. Global, regional, and national disease burden estimates of acute lower respiratory infections due to respiratory syncytial virus in young children in 2015: a systematic review and modelling study. *Lancet* **390**, 946–958 (2017).
- Gaajetaan, G. R. et al. Interferon-beta induces a long-lasting antiviral state in human respiratory epithelial cells. *J. Infect.* **66**, 163–169 (2013).
- Drori, Y. et al. Influenza A virus inhibits RSV infection via a two-wave expression of IFIT proteins. *Viruses* **12**, 1171 (2020).
- George, J. A., AlShamsi, S. H., Alhammadi, M. H. & Alsuwaidi, A. R. Exacerbation of Influenza A Virus Disease Severity by Respiratory Syncytial Virus Co-Infection in a Mouse Model. *Viruses* **13**, 1630 (2021).
- Rossman, J. S. & Lamb, R. A. Influenza virus assembly and budding. *Virology* **411**, 229–236 (2011).
- McCurdy, L. H. & Graham, B. S. Role of plasma membrane lipid microdomains in respiratory syncytial virus filament formation. *J. Virol.* **77**, 1747–1756 (2003).
- Vijaykrishnan, S. et al. Cryotomography of budding influenza A virus reveals filaments with diverse morphologies that mostly do not bear a genome at their distal end. *PLoS Pathog.* **9**, e1003413 (2013).
- Ke, Z. et al. The morphology and assembly of respiratory syncytial virus revealed by cryo-electron tomography. *Viruses* **10**, 446 (2018).
- Conley, M. J. et al. Helical ordering of envelope-associated proteins and glycoproteins in respiratory syncytial virus. *EMBO J.* **41**, e109728 (2022).
- Dee, K. et al. Human rhinovirus infection blocks SARS-CoV-2 replication within the respiratory epithelium: implications for COVID-19 epidemiology. *J. Infect. Dis.* **224**, 31–38 (2021).
- Nickbakhsh, S. et al. Virus–virus interactions impact the population dynamics of influenza and the common cold. *Proc. Natl Acad. Sci. USA* **116**, 27142–27150 (2019).
- Wu, A., Mihaylova, V. T., Landry, M. L. & Foxman, E. F. Interference between rhinovirus and influenza A virus: a clinical data analysis and experimental infection study. *Lancet Microbe* **1**, e254–e262 (2020).
- Cheemarla, N. R. et al. Dynamic innate immune response determines susceptibility to SARS-CoV-2 infection and early replication kinetics. *J. Exp. Med.* **218**, e20210583 (2021).
- Meskill, S. D., Revell, P. A., Chandramohan, L. & Cruz, A. T. Prevalence of co-infection between respiratory syncytial virus and influenza in children. *Am. J. Emerg. Med.* **35**, 495–498 (2017).
- Johnson, J. E., Gonzales, R. A., Olson, S. J., Wright, P. F. & Graham, B. S. The histopathology of fatal untreated human respiratory syncytial virus infection. *Mod. Pathol.* **20**, 108–119 (2007).
- Kuiken, T. & Taubenberger, J. K. Pathology of human influenza revisited. *Vaccine* **26**, D59–D66 (2008).
- Diaz-Munoz, S. L., Sanjuan, R. & West, S. Sociovirology: Conflict, cooperation, and communication among viruses. *Cell Host Microbe* **22**, 437–441 (2017).
- Hui, K. P. et al. Tropism, replication competence, and innate immune responses of influenza virus: an analysis of human airway organoids and ex-vivo bronchus cultures. *Lancet Respir. Med.* **6**, 846–854 (2018).
- Zhang, L., Peeples, M. E., Boucher, R. C., Collins, P. L. & Pickles, R. J. Respiratory syncytial virus infection of human airway epithelial cells is polarized, specific to ciliated cells, and without obvious cytopathology. *J. Virol.* **76**, 5654–5666 (2002).
- Kolesnikova, L. et al. Influenza virus budding from the tips of cellular microvilli in differentiated human airway epithelial cells. *J. Gen. Virol.* **94**, 971–976 (2013).

35. Mohler, L., Flockerzi, D., Sann, H. & Reichl, U. Mathematical model of influenza A virus production in large-scale microcarrier culture. *Biotechnol. Bioeng.* **90**, 46–58 (2005).
36. Bruce, E. A., Digard, P. & Stuart, A. D. The Rab11 pathway is required for influenza A virus budding and filament formation. *J. Virol.* **84**, 5848–5859 (2010).
37. Utley, T. J. et al. Respiratory syncytial virus uses a Vps4-independent budding mechanism controlled by Rab11-FIP2. *Proc. Natl Acad. Sci. USA* **105**, 10209–10214 (2008).
38. Lyles, D. S. Assembly and budding of negative-strand RNA viruses. *Adv. Virus Res* **85**, 57–90 (2013).
39. Chlanda, P. et al. Structural analysis of the roles of influenza A virus membrane-associated proteins in assembly and morphology. *J. Virol.* **89**, 8957–8966 (2015).
40. Kiss, G. et al. Structural analysis of respiratory syncytial virus reveals the position of M2-1 between the matrix protein and the ribonucleoprotein complex. *J. Virol.* **88**, 7602–7617 (2014).
41. Li, Y., Pillai, P., Miyake, F. & Nair, H. The role of viral co-infections in the severity of acute respiratory infections among children infected with respiratory syncytial virus (RSV): A systematic review and meta-analysis. *J. Glob. Health* **10**, 010426 (2020).
42. Calvo, C. et al. Respiratory syncytial virus coinfections with rhinovirus and human bocavirus in hospitalized children. *Medicine* **94**, e1788 (2015).
43. Yoshida, L. M. et al. Respiratory syncytial virus: co-infection and paediatric lower respiratory tract infections. *Eur. Respir. J.* **42**, 461–469 (2013).
44. Ruuskanen, O., Lahti, E., Jennings, L. C. & Murdoch, D. R. Viral pneumonia. *Lancet* **377**, 1264–1275 (2011).
45. Benfield, C. T., Lyall, J. W., Kochs, G. & Tiley, L. S. Asparagine 631 variants of the chicken Mx protein do not inhibit influenza virus replication in primary chicken embryo fibroblasts or in vitro surrogate assays. *J. Virol.* **82**, 7533–7539 (2008).
46. Kremer, J. R., Mastronarde, D. N. & McIntosh, J. R. Computer visualization of three-dimensional image data using IMOD. *J. Struct. Biol.* **116**, 71–76 (1996).
47. Mastronarde, D. N. Automated electron microscope tomography using robust prediction of specimen movements. *J. Struct. Biol.* **152**, 36–51 (2005).
48. Zheng, S. Q. et al. MotionCor2: anisotropic correction of beam-induced motion for improved cryo-electron microscopy. *Nat. Methods* **14**, 331–332 (2017).
49. Bepler, T., Kelley, K., Noble, A. J. & Berger, B. Topaz-Denoise: general deep denoising models for cryoEM and cryoET. *Nat. Commun.* **11**, 5208 (2020).
50. R Core Team. *R: A Language and Environment for Statistical Computing* (2013).
51. Wickham, H. Elegant graphics for data analysis. *Media* **35**, 1007 (2009).

Acknowledgements

This work was supported by grants from the Medical Research Council of the United Kingdom (MC_UU_12014/9 to P.R.M., MR/N013166/1

to J.H., MR/R502327/1 to D.M.G., MC_UU_12014/7 to S.V., and MC_UU_12014/7 to D.B.). The Scottish Centre for Macromolecular Imaging is funded by the Medical Research Council of the United Kingdom (MC_PC_17135) and the Scottish Funding Council (H17007).

Author contributions

Author contributions are based on the CRediT taxonomy (<https://casrai.org/credit/>). J.H.: investigation, methodology, formal analysis, visualization, writing—original draft. S.V.: investigation, data curation, formal analysis, resources, methodology, validation, visualization, supervision, writing—original draft. J.S.: investigation, writing—review and editing. K.D.: investigation, writing—review and editing. D.M.G.: investigation, writing—review and editing. M.C.: investigation, writing—review and editing. M.M.: investigation, methodology, writing—review and editing. S.D.C.: formal analysis, writing—review and editing. D.B.: resources, funding acquisition, writing—review and editing. P.R.M.: conceptualization, methodology, validation, data curation, supervision, funding acquisition, project administration, writing—original draft.

Competing interests

The authors declare no competing interests.

Additional information

Extended data is available for this paper at <https://doi.org/10.1038/s41564-022-01242-5>.

Supplementary information The online version contains supplementary material available at <https://doi.org/10.1038/s41564-022-01242-5>.

Correspondence and requests for materials should be addressed to Pablo R. Murcia.

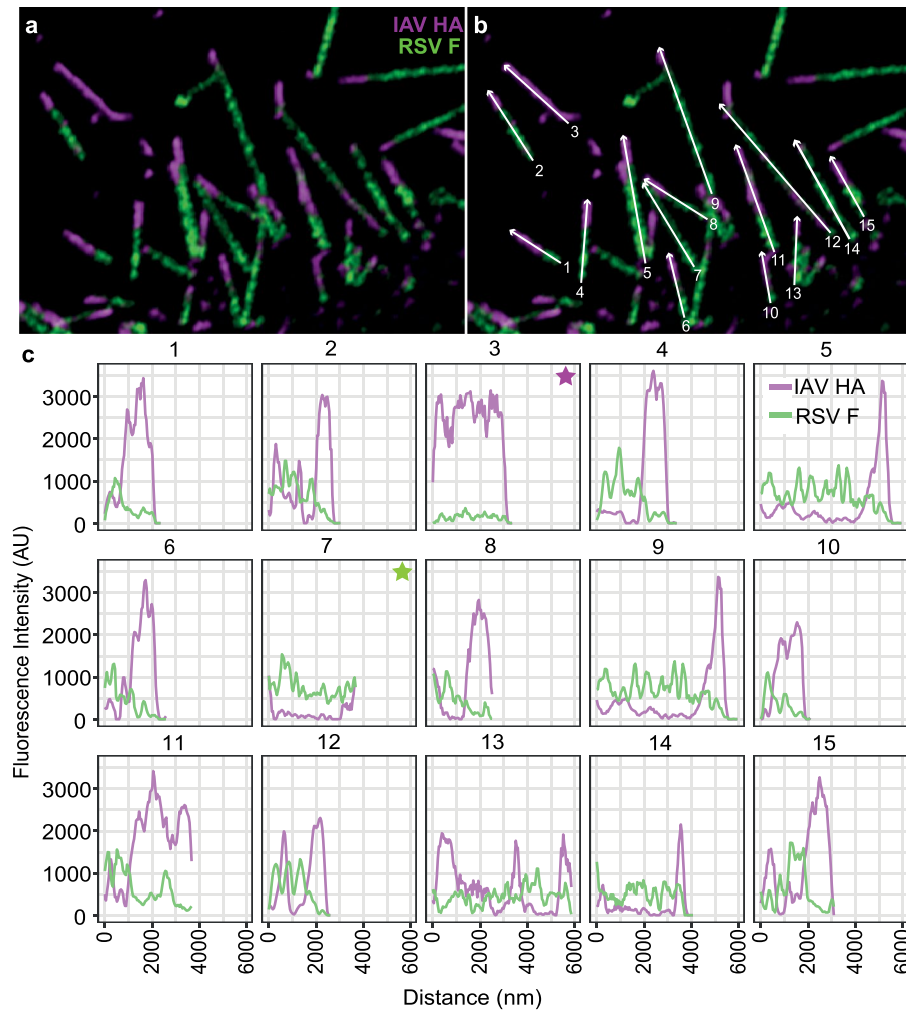
Peer review information *Nature Microbiology* thanks Ultan Power and the other, anonymous, reviewer(s) for their contribution to the peer review of this work. Peer reviewer reports are available.

Reprints and permissions information is available at www.nature.com/reprints.

Publisher's note Springer Nature remains neutral with regard to jurisdictional claims in published maps and institutional affiliations.

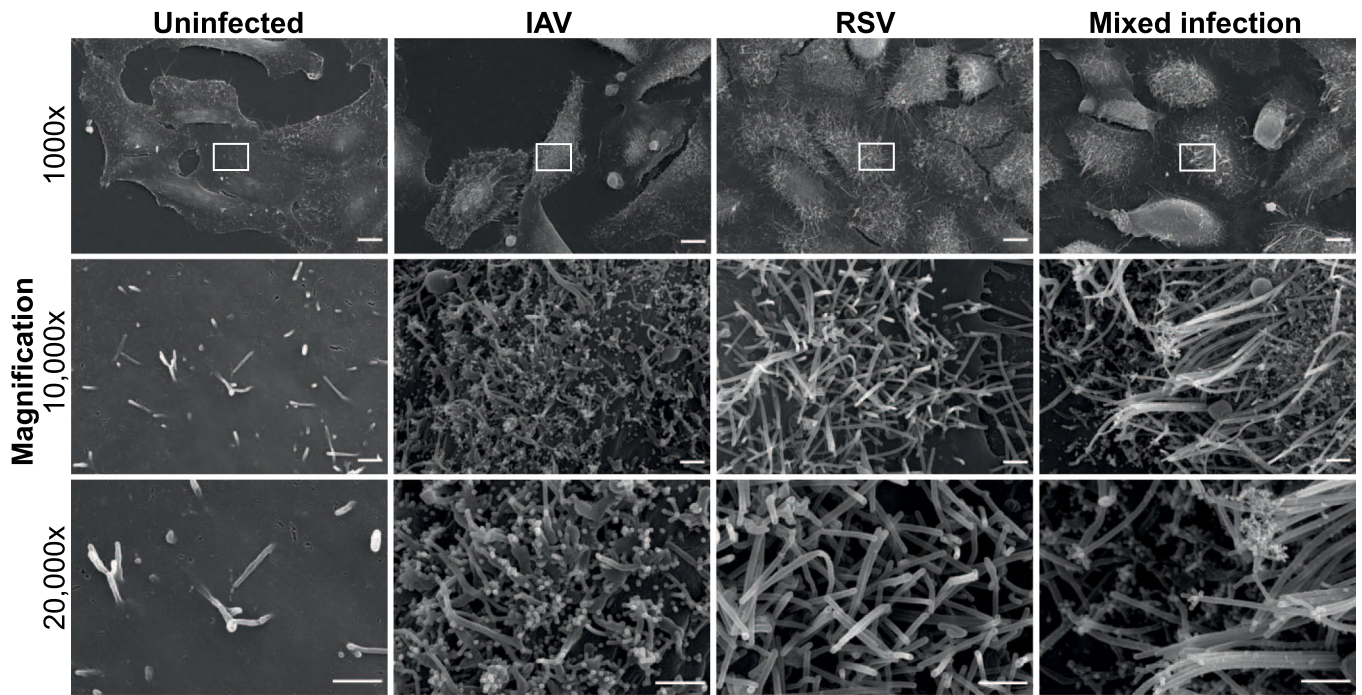
Springer Nature or its licensor holds exclusive rights to this article under a publishing agreement with the author(s) or other rightsholder(s); author self-archiving of the accepted manuscript version of this article is solely governed by the terms of such publishing agreement and applicable law.

© The Author(s), under exclusive licence to Springer Nature Limited 2022



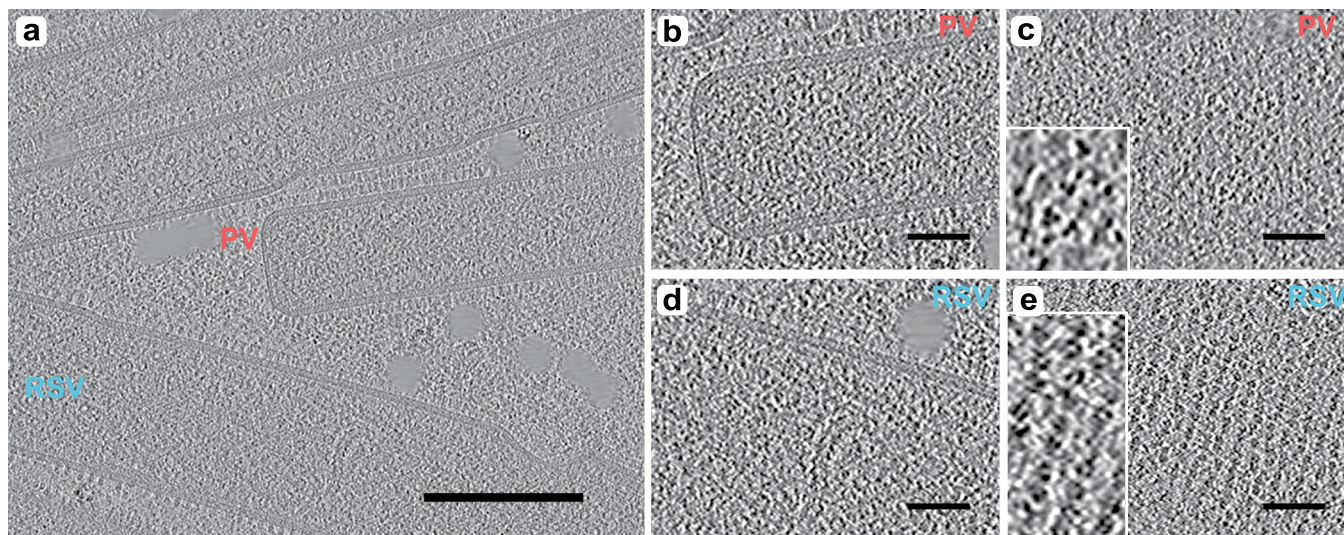
Extended Data Fig. 1 | HA and F are expressed in discrete patches along the length of filaments, with HA predominantly at the distal end. (a) Magnified view of cell associated filaments (full image shown in Fig. 2A) show filaments with distinct patches of IAV HA (magenta) and RSV F (green) glycoproteins along the length of the filaments. **(b)** White arrows and filament numbering correspond

to fluorescence intensity profiles displayed in (c). Minimal colocalisation was observed in the fluorescence intensity profiles (c) for IAV HA (magenta line) and RSV F (green line) signal along filaments numbered 1–15. IAV (filament 3, magenta star) and RSV (filament 7, green star) filaments were also identified among dual positive filaments.



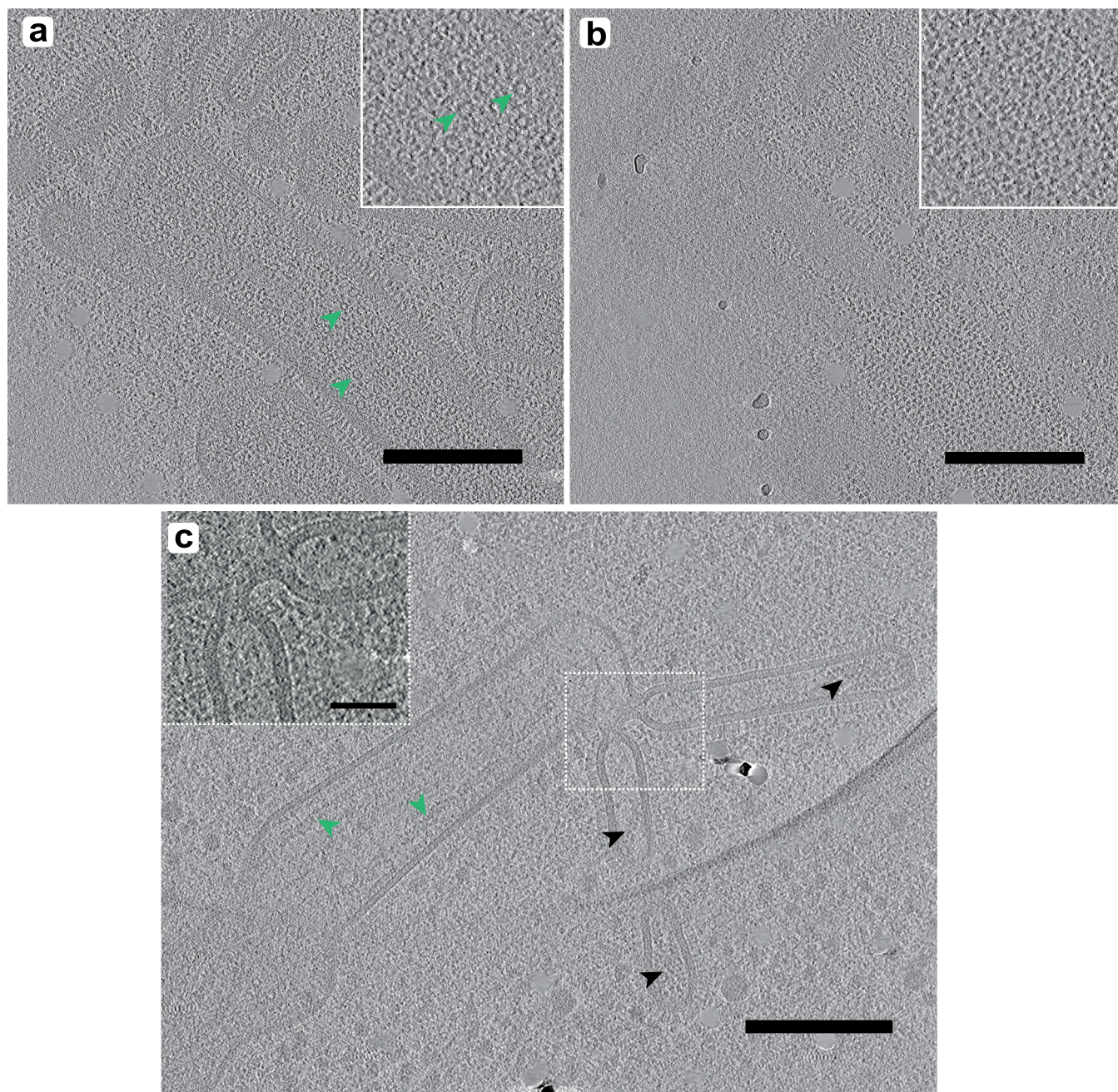
Extended Data Fig. 2 | Scanning electron microscopy shows clear differences between IAV and RSV virion structure. Scanning electron micrographs of IAV, RSV, coinfecting or mock infected cells imaged at 1000x (top row), 10,000x (middle row) and 20,000x (bottom row), region of magnification is denoted

by the white box. Scale bars represent 10 μm at 1000x and 1 μm at 10,000x and 20,000x magnification. Micrographs representative of $n = 2$ biologically independent experiments.



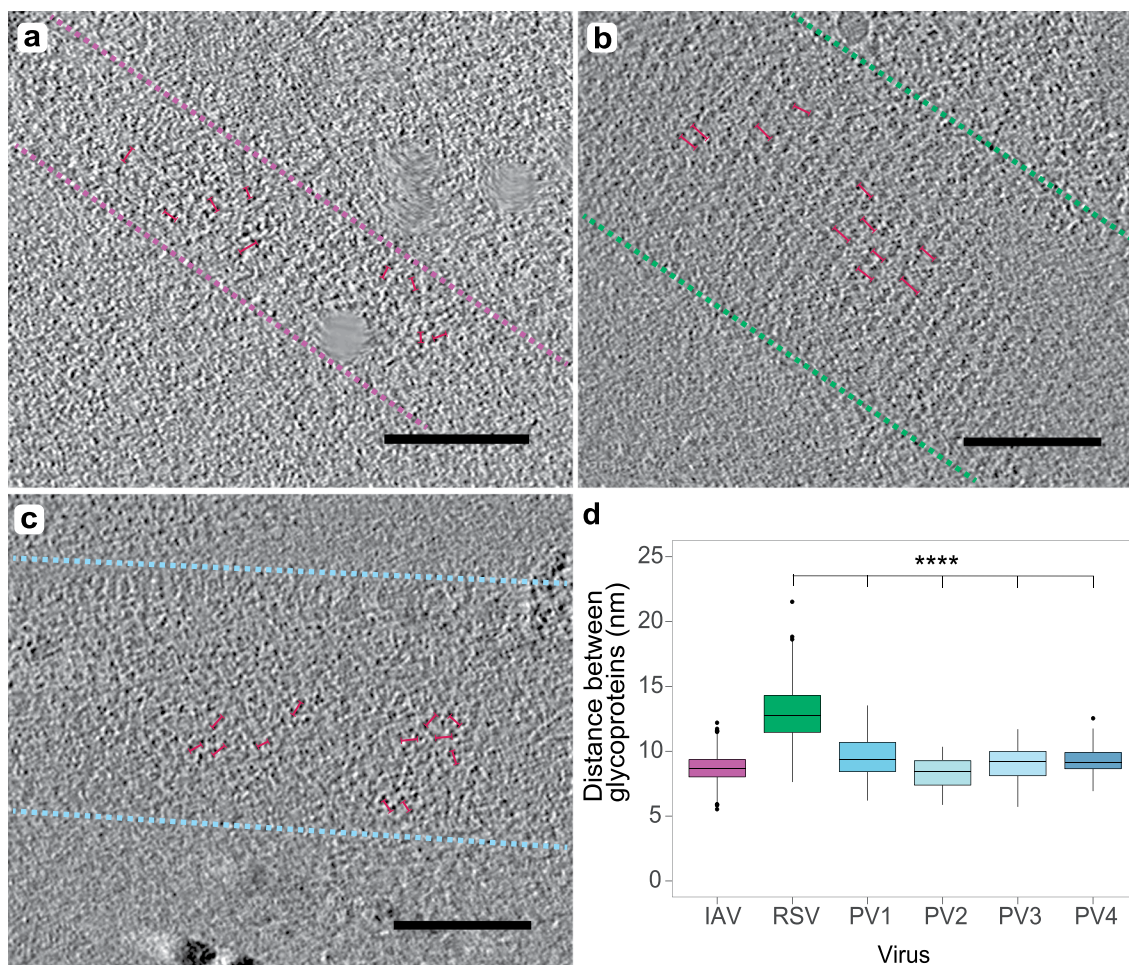
Extended Data Fig. 3 | Coinfection generates RSV filaments that are pseudotyped with IAV envelope proteins. (a) Tomogram shows a pseudotyped RSV filament, indicated by red 'PV' label, near to RSV filaments, one example indicated by blue 'RSV' label. Scale bar indicates 200 nm. (b) Magnified cross-section of end of pseudotyped filament, showing RSV RNP contained within virion. (c) Surface of pseudotyped filament shows irregular arrangement of glycoproteins, with many displaying characteristic triangular shape of HA

trimers, shown in magnified inset image. (d) Magnified cross-section of end of RSV filament, showing RSV RNP contained within virion and ultra-structure consistent with the pseudotyped virion. (e) Surface of the RSV filament shows helical arrangement of glycoproteins, with ring-shaped density of glycoproteins highlighted in magnified insert. Scale bars in panels (c-e) indicate 50 nm. Micrographs shown in (a-e) representative of $n = 3$ biologically independent experiments.



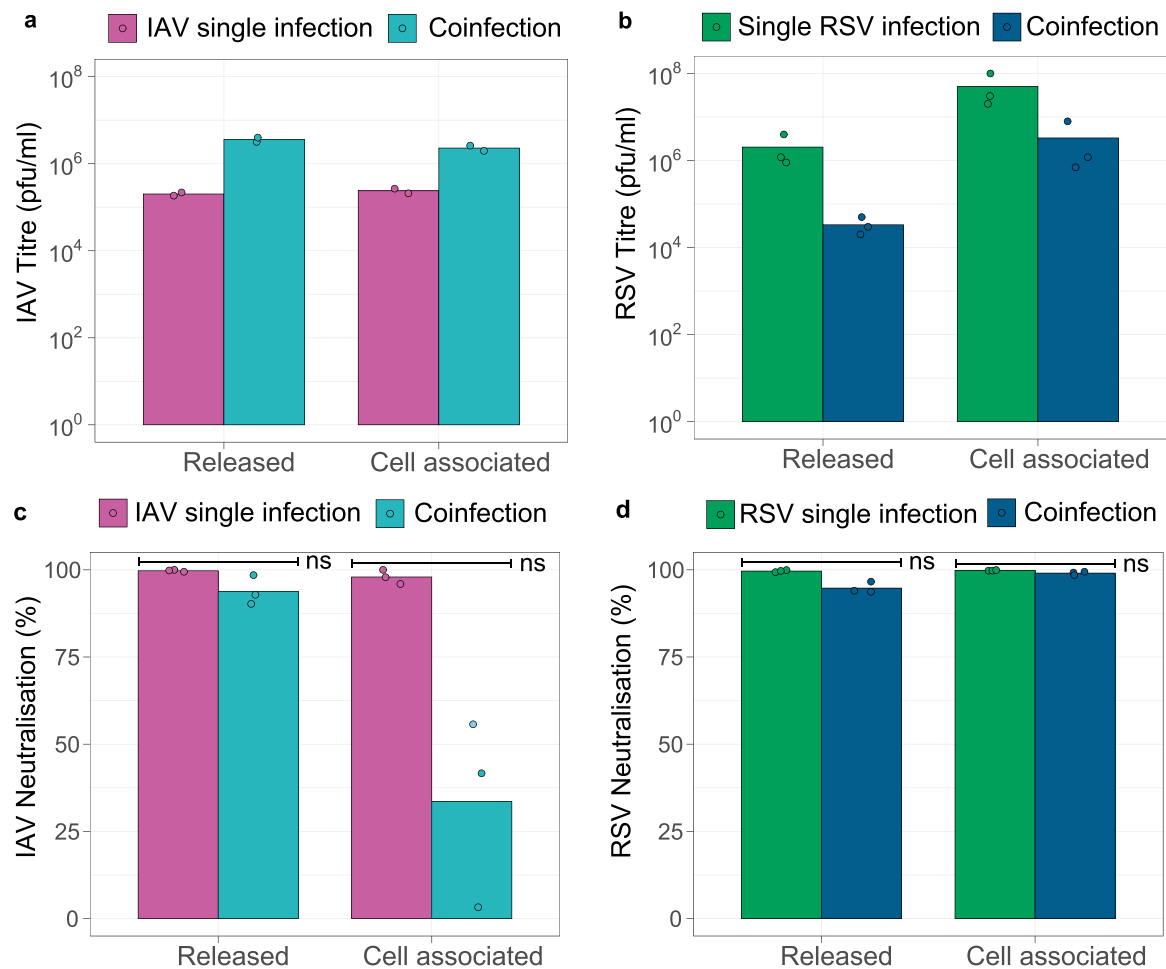
Extended Data Fig. 4 | Further examples of hybrid particles. (a and b) show two z-positions through the same hybrid particle, which also displays pseudotyping in RSV-like region. (a) IAV-like regions extend from the top of the filament and ring-shaped densities corresponding to RSV genome, indicated by green arrows and highlighted in magnified inset image, are present within the virion. (b) The surface of the virion is covered in glycoproteins that are consistent in shape and arrangement with IAV glycoproteins, highlighted in magnified inset. Scale bars indicate 200 nm. (c) Tomogram shows a further example of a

hybrid particle with two IAV-like regions which are joined to the RSV-like region by a continuous membrane. Black and green arrows indicate IAV and RSV RNP respectively, contained within their associated structural regions. Scale bar indicates 200 nm. There is a clear shared lumen which continues between RSV and IAV regions, highlighted within magnified inset which corresponds to region marked by white dashed box. Scale bar indicates 50 nm. Micrographs shown in (a-c) representative of $n = 3$ biologically independent experiments.



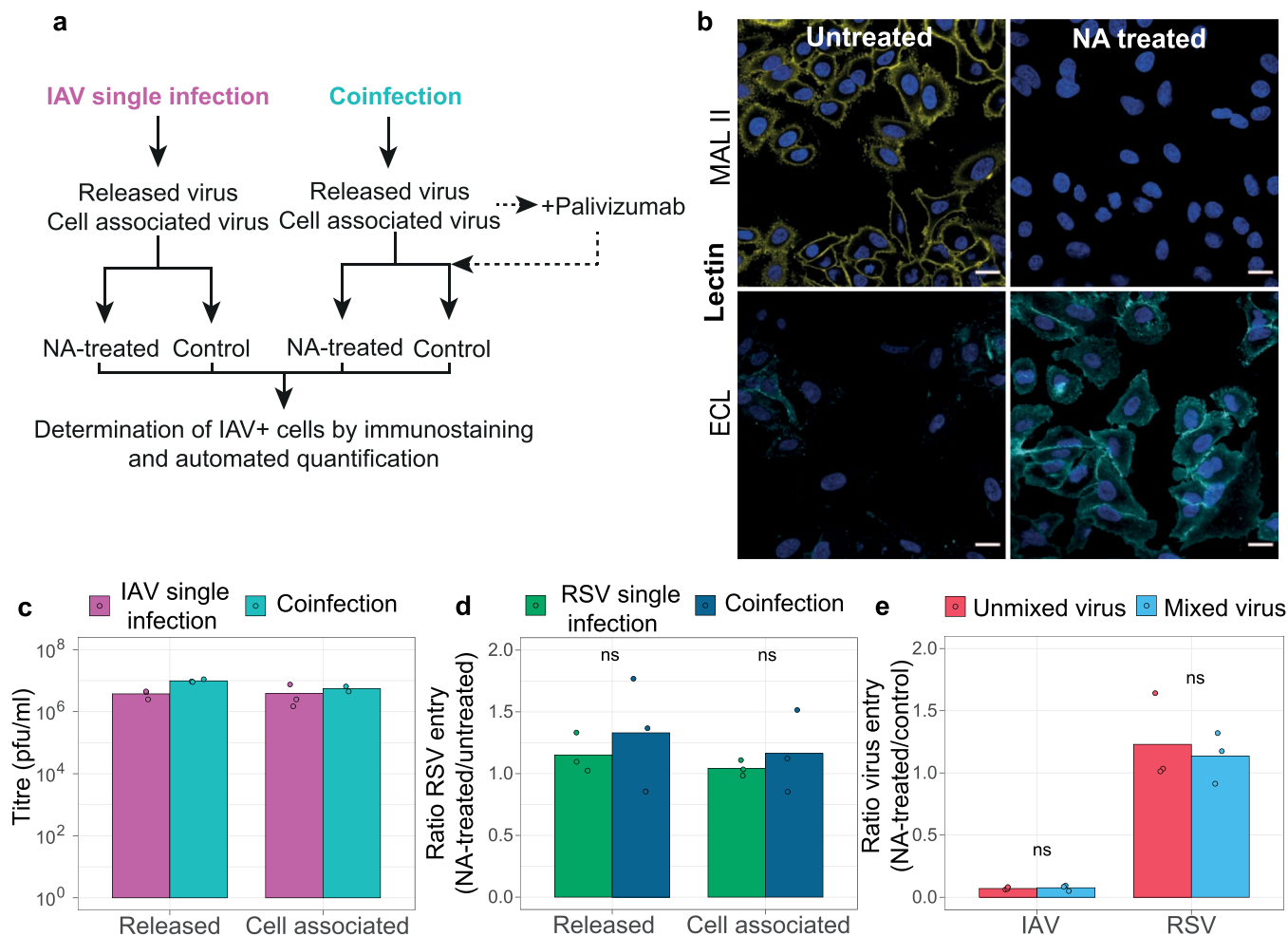
Extended Data Fig. 5 | Inter-spike distance measurements reveal that pseudotyped viruses are decorated with IAV glycoproteins. To determine the glycoprotein arrangement on pseudotyped viruses, inter-spike distances were measured between glycoprotein pairs. Representative examples are shown for IAV (**a**), RSV (**b**) and pseudotyped virions (**c**) with red lines indicating example distances measured. Pink, green and blue dashed lines indicate the edges of IAV, RSV and pseudotyped filaments respectively. Scale bars indicate 200 nm. (**d**) Tomography data was collected from $n = 2$ biologically independent experiments. Control measurements were collected from 11 tomograms for IAV

(measurements $n = 326$) and 11 tomograms for RSV (measurements $n = 236$). Measurements of pseudotyped virions were collected from 4 individual tomograms ($n = 50$ measurements per tomogram). Average inter-spike distances were 8.71 nm for IAV, 12.9 nm for RSV and a range of 8.31–9.56 nm for pseudotypes. Statistical significance was determined by two tailed unpaired t-test analysis, **** $p < 0.0001$. Box plot shows interquartile range (25th percentile, median, 75th percentile), whiskers represent minimum and maximum values and black points represent outliers.



Extended Data Fig. 6 | Hybrid viral particles evade neutralizing antibodies against IAV, but not RSV. Virus harvested from coinfection or single infections was pre-incubated with serum targeting IAV HA, RSV F or a serum-free control, and then used to infect A549 cells. Infections were fixed and immunostained at 12 hpi and the number of IAV infected cells was quantified using an automated image-based cell counter. The same virus stocks were back titrated to determine infectious viral input. **(a)** Back titration of IAV in single infection (magenta bars) or coinfection (teal bars) by IAV plaque assay. **(b)** Back titration of RSV in single infection (green bars) or coinfection (dark blue bars) by RSV plaque assay. **(c)** Neutralisation of IAV by polyclonal antisera targeting IAV HA when virus was harvested from the supernatant or cell pellet fractions of a single IAV infection

(magenta bars) or a coinfection (teal bars). Neutralisation was calculated as a percentage of IAV infected cells in the wells containing serum compared to matched serum-free controls. **(d)** Neutralisation of RSV by Palivizumab (targeting RSV F) when virus was harvested from the supernatant or cell pellet fractions of a single RSV infection (green bars) or a coinfection (dark blue bars). Neutralisation calculated as a percentage of RSV infected cells in the wells containing serum compared to matched serum-free controls. Data shown in **(a-d)** was collected from $n = 3$ independent experiments and statistical significance calculated by two tailed Mann Whitney test, ns indicates $p > 0.05$. Bars represent mean and data points represent biological replicates.



Extended Data Fig. 7 | Supporting data for neuraminidase experiment. (a) Schematic demonstrating experimental design. **(b)** NA-treated and untreated cells stained with Maackia Amurensis Lectin II (MAL II) in yellow (top row) and Erythrina Cristagalli Lectin (ECL) in cyan (bottom row). Scale bar represents 20 μm . Images representative of $n = 2$ biologically independent experiments. **(c)** Viral input in pfu/ml of IAV as determined by back-titration of inoculum for NA-experiment by IAV plaque assay. **(d)** Ratio of RSV entry into NA-treated cells versus control cells when harvested from single infection (green bars) or mixed

infection (blue bars). RSV entry to NA-treated cells was calculated as a percentage of the RSV-positive cell count in the matched untreated control. **(e)** Ratio of virus entry of IAV only or RSV only (red bars) into NA-treated over control cells, compared to entry of IAV pre-mixed with RSV or RSV pre-mixed with IAV into NA-treated over control cells (blue bars). Data shown in **(c-e)** was collected from $n = 2$ **(c)** or 3 **(d-e)** independent experiments and statistical significance calculated by two tailed Mann Whitney test, ns indicates $p > 0.05$. Bars represent mean and data points represent biological replicates.

Reporting Summary

Nature Portfolio wishes to improve the reproducibility of the work that we publish. This form provides structure for consistency and transparency in reporting. For further information on Nature Portfolio policies, see our [Editorial Policies](#) and the [Editorial Policy Checklist](#).

Statistics

For all statistical analyses, confirm that the following items are present in the figure legend, table legend, main text, or Methods section.

- | | |
|-------------------------------------|--|
| n/a | Confirmed |
| <input type="checkbox"/> | <input checked="" type="checkbox"/> The exact sample size (n) for each experimental group/condition, given as a discrete number and unit of measurement |
| <input type="checkbox"/> | <input checked="" type="checkbox"/> A statement on whether measurements were taken from distinct samples or whether the same sample was measured repeatedly |
| <input type="checkbox"/> | <input checked="" type="checkbox"/> The statistical test(s) used AND whether they are one- or two-sided
<i>Only common tests should be described solely by name; describe more complex techniques in the Methods section.</i> |
| <input checked="" type="checkbox"/> | <input type="checkbox"/> A description of all covariates tested |
| <input type="checkbox"/> | <input checked="" type="checkbox"/> A description of any assumptions or corrections, such as tests of normality and adjustment for multiple comparisons |
| <input type="checkbox"/> | <input checked="" type="checkbox"/> A full description of the statistical parameters including central tendency (e.g. means) or other basic estimates (e.g. regression coefficient) AND variation (e.g. standard deviation) or associated estimates of uncertainty (e.g. confidence intervals) |
| <input type="checkbox"/> | <input checked="" type="checkbox"/> For null hypothesis testing, the test statistic (e.g. F , t , r) with confidence intervals, effect sizes, degrees of freedom and P value noted
<i>Give P values as exact values whenever suitable.</i> |
| <input checked="" type="checkbox"/> | <input type="checkbox"/> For Bayesian analysis, information on the choice of priors and Markov chain Monte Carlo settings |
| <input checked="" type="checkbox"/> | <input type="checkbox"/> For hierarchical and complex designs, identification of the appropriate level for tests and full reporting of outcomes |
| <input checked="" type="checkbox"/> | <input type="checkbox"/> Estimates of effect sizes (e.g. Cohen's d , Pearson's r), indicating how they were calculated |

Our web collection on [statistics for biologists](#) contains articles on many of the points above.

Software and code

Policy information about [availability of computer code](#)

Data collection Confocal data collected using Zeiss Zen Black version 14.0.24.201 and Zeiss Zen Blue version 2.6.76. Scanning electron data collected using InTouch Scope software version 1.05. Cryo-electron tomography data collected using SerialEM version 4.0.3.

Data analysis Images processed using ImageJ, version v2.0.0-rc-56/1.52g. Tomography data was motion corrected using MotionCor2 version 1.4.7 and analysed using IMOD version 4.11. Data analysed using Graphpad Prism version 9.1.0 and visualised in R Studio version 1.3.1056.

For manuscripts utilizing custom algorithms or software that are central to the research but not yet described in published literature, software must be made available to editors and reviewers. We strongly encourage code deposition in a community repository (e.g. GitHub). See the Nature Portfolio [guidelines for submitting code & software](#) for further information.

Data

Policy information about [availability of data](#)

All manuscripts must include a [data availability statement](#). This statement should provide the following information, where applicable:

- Accession codes, unique identifiers, or web links for publicly available datasets
- A description of any restrictions on data availability
- For clinical datasets or third party data, please ensure that the statement adheres to our [policy](#)

Representative tomograms of the chimeric virus particles described in this paper have been deposited in the Electron Microscopy Data Bank (www.ebi.ac.uk/emdb) under accession codes EMD-13228 and EMD-13229.

Field-specific reporting

Please select the one below that is the best fit for your research. If you are not sure, read the appropriate sections before making your selection.

Life sciences Behavioural & social sciences Ecological, evolutionary & environmental sciences

For a reference copy of the document with all sections, see [nature.com/documents/nr-reporting-summary-flat.pdf](https://www.nature.com/documents/nr-reporting-summary-flat.pdf)

Life sciences study design

All studies must disclose on these points even when the disclosure is negative.

Sample size	No sample size calculations were performed, but for all statistical analysis data was collected from biologically independent experiments. For all quantitative experiments, a minimum of three biologically independent experiments consisting of three technical replicates. This sample size was selected as this was the minimum sample size required to calculate variance between experiments. For transwell experiments, three biologically independent replicates were used, each consisting of two technical replicates (two independent transwells) due to availability of primary cells.
Data exclusions	No data was excluded from the analysis, unless measurements had failed due to technical issues.
Replication	Typically three independent experiments were carried out for all experimental data included, with reproducible results between experiments. Electron microscopy imaging experiments were carried out twice independently, with a minimum of duplicate samples per experimental condition.
Randomization	Randomization was not applicable for any experiments described. Virus titrations to quantify viral replication does not require random sampling. For immunofluorescence and electron microscopy experiments, we selected areas with evidence of coinfection or hybrid viral particles which was the objective of these experiments.
Blinding	Due to the cytopathic effect induced by viral infections, it was immediately obvious which sample was infected with each virus, therefore blinding was not possible for most experiments in the study. Blinding was used in the to collect the data shown in figure 1B where areas for imaging were selected based on nuclear density (using DAPI staining), without viewing antigen positivity prior to collecting the images.

Reporting for specific materials, systems and methods

We require information from authors about some types of materials, experimental systems and methods used in many studies. Here, indicate whether each material, system or method listed is relevant to your study. If you are not sure if a list item applies to your research, read the appropriate section before selecting a response.

Materials & experimental systems

n/a	Involved in the study
<input type="checkbox"/>	<input checked="" type="checkbox"/> Antibodies
<input type="checkbox"/>	<input checked="" type="checkbox"/> Eukaryotic cell lines
<input checked="" type="checkbox"/>	<input type="checkbox"/> Palaeontology and archaeology
<input checked="" type="checkbox"/>	<input type="checkbox"/> Animals and other organisms
<input checked="" type="checkbox"/>	<input type="checkbox"/> Human research participants
<input checked="" type="checkbox"/>	<input type="checkbox"/> Clinical data
<input checked="" type="checkbox"/>	<input type="checkbox"/> Dual use research of concern

Methods

n/a	Involved in the study
<input checked="" type="checkbox"/>	<input type="checkbox"/> ChIP-seq
<input checked="" type="checkbox"/>	<input type="checkbox"/> Flow cytometry
<input checked="" type="checkbox"/>	<input type="checkbox"/> MRI-based neuroimaging

Antibodies

Antibodies used	Primary antibodies: RSV fusion glycoprotein (Abcam, UK, AB24011, 1/1000), RSV nucleoprotein (Abcam, UK, AB22501, 1/1500), antisera to influenza A H1 (A/Puerto Rico/8/34, 1/1000) (NIBSC, UK, 03/242), influenza A virus nucleoprotein (European Veterinary Society, EVS238, 1/1000), IAV (A/Puerto Rico/8/34) HA (Sinobiological, 11684-MM03, 1/500), polyclonal anti-IAV (A/Puerto Rico/8/34) nucleoprotein kindly provided by Paul Digard, goat polyclonal anti-RSV (Abcam, AB20745, 1/500). Secondary antibodies: Rabbit anti-mouse IgG alexafluor 488 conjugate (Sigma-Aldrich, USA, SAB4600056, 1/1000), donkey anti-mouse 594 conjugate (Abcam, UK, ab150108, 1/1000) donkey anti-sheep alexafluor 594 conjugate (Thermo Fisher Scientific, USA, A-11016, 1/1000), goat anti-rabbit alexafluor 488 (Invitrogen, A11034, 1/500).
Validation	Prior to application in experiments, all antibodies were optimised and checked for cross-reactivity antibodies used in co-staining protocols. Manufacturers validations/citing references -RSV fusion glycoprotein (Abcam, UK, AB24011) - Mouse monoclonal antibody. Validated for use in IF/ICC against RSV A/2. Use for immunofluorescence cited in: DOI:10.1111/jcmm.15845, DOI:10.1002/jcb.28902, DOI:10.1186/s12929-018-0416-6. - RSV nucleoprotein (Abcam UK, AB22501) - Mouse monoclonal antibody. Validated for used against RSV A/2. Use for

immunofluorescence cited in: DOI:10.1038/s41467-017-00732-z, DOI:10.1038/lsa.2016.134.
 - Anti-RSV (Abcam, AB20745) - Validated for use in ICC/IF. Use cited for IF cited: <https://doi.org/10.7554/eLife.42448>
 - Antisera to influenza A H1 (A/Puerto Rico/8/34) (NIBSC, UK, 03/242) - Sheep polyclonal antibody raised against purified HA antigen. Use cited: <https://doi.org/10.1002/bit.27876>.
 - Influenza A virus nucleoprotein (European Veterinary Society, EVS-238) - Mouse monoclonal antibody. Use cited: <https://doi.org/10.1186/1297-9716-42-10>.
 - Influenza A virus H1N1 haemagglutinin (Sinobiological, 11684-MM03) - Mouse monoclonal antibody. Validated for use against A/Puerto Rico/8/34 for western blot and ELISA. Use cited: DOI:10.1016/j.virol.2018.11.010

Eukaryotic cell lines

Policy information about [cell lines](#)

Cell line source(s)	Human lung adenocarcinoma cells (A549) (American Type Culture Collection [ATCC], CCL-185), Madin Darby canine kidney (MDCK) cells (ATCC, CCL-34), HEp-2 (ATCC, CCL-23). Primary human bronchial epithelial cells from a Caucasian male donor (EpithelixSarl, 02AB077201F2)
Authentication	No cell lines used were authenticated
Mycoplasma contamination	Cell lines tested negative for mycoplasma contamination using MycoAlert® Mycoplasma Detection Kit
Commonly misidentified lines (See ICLAC register)	HEp-2 cells (ATCC, CCL-23) were used in this study and were not authenticated before use. These cells were used specifically to grow RSV virus stocks and titrate RSV samples as this cell line is highly permissive to infection by RSV and is used as standard to propagate RSV propagation virus stocks. Use of HEp-2 cited in the following: DOI: 10.3791/59218, https://doi.org/10.1007/978-1-4939-3687-8_3 , DOI: 10.1016/j.jviromet.2004.02.020.